The Dissertation Committee for Jichul Shin
certifies that this is the approved version of the following dissertation:

A study of direct-current surface discharge plasma for a Mach 3 supersonic flow control

Committee:

Laxminarayan L. Raja, Supervisor

Noel T. Clemens

Philip L. Varghese

Roger D. Bengtson

Ofodike A. Ezekoye

A study of direct-current surface discharge plasma for a Mach 3 supersonic flow control

by

Jichul Shin, B.Eng; M.S.

DISSERTATION

Presented to the Faculty of the Graduate School of

The University of Texas at Austin

in Partial Fulfillment

of the Requirements

for the Degree of

DOCTOR OF PHILOSOPHY

THE UNIVERSITY OF TEXAS AT AUSTIN

August 2007

To my parents, Hyunsuk Shin and Eunhee Cho, to my wife, Hyejin Park, to my brother, Sungchul Shin, and to my sister, Jina Shin for their steadfast trust and love.

Acknowledgments

I wish to thank the multitudes of people who helped me in the course of this study. Best thanks to my advisor, Prof. Laxminarayan L. Raja for academic advice and steady encouragement on this accomplishment. I am grateful to my committee members, Prof. Noel T. Clemens, Prof. Philip L. Varghese, Prof. Roger D. Bengtson, and Prof. Ofodike A. Ezekoye for their invaluable advice. I thank Venkat Narayanaswamy for helping me making experiment and for making valuable discussions. I also thank my colleagues, Prashanth S. Kothnur, Xiaohui Yuan, Guangye Chen, Shankar Mahadevan and Thomas Deconinck for their cares and inputs on my research.

A study of direct-current surface discharge plasma for a Mach 3 supersonic flow control

Publication No. _____

Jichul Shin, Ph.D.
The University of Texas at Austin, 2007

Supervisor: Laxminarayan L. Raja

A direct-current, non-equilibrium surface glow discharge plasma in the presence of a Mach 2.85 flow is studied experimentally for flow control applications. The discharge is generated with pin-like electrodes flush mounted on a ceramic plate with sustaining currents from 25 mA to 300 mA. In the presence of a supersonic flow, two distinct discharge modes - diffuse and constricted - are observed depending on the flow and discharge operating conditions. In cathode upstream location, both diffuse and constricted discharges are observed while in cathode downstream location, the discharge mostly exhibits either constricted mode or bistable mixed mode. The effect of the discharge on the flow ("plasma actuation") is characterized by the appearance of a weak shock wave in the vicinity of the discharge. The shock is observed at low powers ($\sim$10 W) for the diffuse discharge mode but is absent for the higher power ($\sim$100 W) constricted mode. High speed laser schlieren imaging suggests that the diffuse mode plasma actuation is rapid as it occurs on a time scale that is

less than 100 μsec. Rotational (gas) and vibrational temperatures within the discharge are estimated by emission spectral line fits of N_2 and N_2^+ rovibronic bands near 365-395 nm. The electronic temperatures are estimated by using the Boltzmann plot method for Fe(I) atomic lines. Rotational temperatures are found to be high ($\sim$1500 K) in the absence of a flow but drop sharply ($\sim$500 K) in the presence of a supersonic flow for both the diffuse and constricted discharge modes. The vibrational and electronic temperatures are measured to be about 3000 K and 1.25 eV (14500 K), respectively, and these temperatures are the same with and without flow. The gas (rotational) temperature spatial profiles above the cathode surface are found to be similar for the diffuse and constricted modes indicating that dilatational effects due to gas heating are similar. However, complete absence of flow actuation for the constricted mode suggests that electrostatic forces may also play an important role in supersonic plasma-flow actuation phenomena. Analytical estimates using cathode sheath theory indicates that ion pressure within the cathode sheath can be significant resulting in gas compression in the sheath and a corresponding expansion above it. The expansion in turn may fully negate the dilatational effect in the constricted case resulting in an apparent absence of forcing in the constricted case. Plasma-induced flow velocity reaches about 1 m/s in stagnant air at the discharge current of order tens of milliamps. This electrostatic forcing in the direction from anode to cathode can play an important role in the boundary layer of supersonic flow.

Table of Contents

List of Tables

List of Figures

List of Symbols

E	Electric field [V/m] or Energy [J]
V	applied voltage [V]
I	discharge current [A]
J_o	current density [A/m^2]
M	ion mass [kg]
n_i	ion number density [m^{-3}]
n_e	electron number density [m^{-3}]
n_g	background gas number density [m^{-3}]
u_i	ion drift velocity [m/s]
σ	collision crossection [m^2]
P	pressure [Pa]
T_r	rotational temperature [K]
T_v	vibrational temperature [K]
T_e	electronic temperature [K] or [eV]
μ_i	ion mobility
e	unit charge
ε_o	vacuum permittivity
t_s	sheath thickness [m]
ρ	space charge density
λ_{Debye}	Debye length [m]
λ	mean free path [m]
Re	Reynolds number
k	Boltzmann constant [J/K]
J	total angular momentum
K	total angular momentum apart from spin ($J = K + S$)
S	spin quantum number
N	projection of J to right angles to the internuclear axis
Λ	quantum number of the angular momentum of the electrons about internuclear axis
ψ	total eigenfunction of Schrodinger equation
ψ_e	electronic eigenfunction
ψ_v	vibrational eigenfunction
ψ_r	rotational eigenfunction
h	Planck constant, 6.626068$\times$ 10^{-34} [kg m^2/s]
ν	transition frequency
I_{em}	spectral emission line intensity

$A'_{\prime\prime}$	Einstein coefficient of spontaneous emission
$(R'_{\prime\prime})^2$	Electronic-vibrational transition moment
δ	Kronecker delta
Ψ	vibrational wave function
$R_e(r)$	electronic transition moment function (ETMF)
$q'_{\prime\prime}$	Frank-Condon factor
$S_{v'v''}$	band strength
S	spin quantum number
N_o	total number density of upper state
$N_{n'}$	number density of upper electronic state
$N_{n'v'}$	number density of upper vibrational state
$N_{n'v'J'}$	number density of upper rotational state
E_e	energy in electronic state [J]
E_v	energy in vibrational state [J]
E_r	energy in rotational state [J]
Q_{el}	partition function of electronic state
Q_v	partition function of vibrational state
Q_r	partition function of rotational state
$g_{J'}$	degeneracy of rotational state(i.e. line strength)
B_v, D_v	rotational constants
F	energy term [cm^{-1}]
M	Mach number
T_o	stagnation temperature [K]
P_o	stagnation pressure [Torr, Pa]
x	streamwise location [m]
u_∞	free stream velocity [m/s]
ρ_∞	free stream density [$\mathrm{kg/m}^3$]
P_∞	free stream pressure [Torr, Pa]
T_∞	free stream temperature [K]
Re_x	local Reynolds number
C_f	friction coefficient
u^*	friction velocity [m/s]
ρ_w	gas density at the wall [$\mathrm{kg/m}^3$]

Chapter 1

Introduction

Plasmas are ionized gases and can be generated in various types of discharge configurations. In particular, non-equilibrium plasmas, where the temperature of electrons and ions are significantly different, are very widely used in industry and research laboratories. For example, inductively-coupled plasmas (ICP) and capacitively-coupled plasmas (CCP) are commonly used in the semiconductor industry. They use high frequency power sources typically at 13.56 MHz. Direct-current (DC) discharges have been studied for a long time and are best exemplified by the low pressure glow discharge in a vacuum tube. A recent application of DC discharges is the plasma display panel (PDP) [1].

In recent years, plasma-based aerodynamic flow actuation applications have been developed using single dielectric-barrier discharges (DBD) [2–4], DC glow discharges [5–7], DC filamentary discharges [8–11], and RF discharges [12]. The use of plasmas for flow control applications is particularly promising owing to the potential for achieving high-bandwidth actuation without moving mechanical parts. Most importantly, the discharge plasmas can create a direct body force in the bulk flow rather than at the bound-

aries of the flow such as walls or inlets/outlets. Plasma actuation is achieved through one or more of three basic forcing mechanisms: 1) rapid gas heating of the flow achieved by volumetric Joule heating (dilatation effect), 2) electro-hydrodynamic (EHD) forcing by imparting directed momentum to the bulk flow using electrostatic force generated by interaction of charge particles with an external electric field, and 3) magneto-hydrodynamic (MHD) forcing, which relies on the Lorentz force on the bulk flow owing to the interaction of electrical currents with an externally imposed magnetic field.

In low-speed aerodynamic flow applications which are mostly at atmospheric pressures, DBD type actuators with asymmetric electrode/dielectric configurations have been used [2–4, 13]. A major conceptual motivation for using DBD is the fact that it can create a glow discharge at high pressures. Electric charge trapped on a dielectric layer induces an opposing electric field in the discharge such that the discharge is extinguished before the current increases above the threshold for glow-to-arc transition. This prevents the discharge from forming an arc at high pressures. Owing to the current limiting behavior of dielectric covered electrodes, these actuators are characterized by pulsed operation with 1-10 kV applied voltages at frequencies of about 10 kHz and low peak current densities ($\sim$1 A/m^2) [14–16]. DBD discharges generate low (room) temperature plasmas and rely on the EHD forcing mechanism. The main weakness of DBD actuators is the relatively small actuation effect as characterized by the induced flow velocity. For example, Roth [3] and Leonov *et al.* [9] have estimated induced velocities of about 10 m/s and less,

in DBDs. In particular, Leonov *et al.* [9] comment that induced flow velocities higher than about 10 m/s are not possible in practice because increased DBD current results in increased gas heating and surface heating rather than EHD forcing. Results from the numerical studies by Shyy *et al.* [13] support the above estimates; they found that the maximum induced flow speeds were approximately 15 m/s and the maximum effect was obtained at very low free stream velocity ($\sim$2 m/s). DBD actuator has been only applied to low speed flows. Recently, the effect of high speed (transonic and supersonic) flow on the performance of DBD discharge has been studied [17]. It was reported that the glow feature in DBD diminishes and filamentary discharge prevails as the flow velocity increases. However, the actuation effect produced by DBD actuator in the presence of supersonic flow was not discussed in the report.

Dilatation effects produced by gas heating in DC discharge have been shown to be much more effective in supersonic flow actuation. For example, Kimmel *et al.* [5] have shown that a diffuse DC glow discharge with an input power of about 50 W in a stream-wise electrode arrangement (with cathode upstream) can increase the surface pressure in the immediate vicinity of the cathode by about 10%. Surface pressure measurements [5] and global force measurements on plasma actuated surfaces [18] showed a linear trend with input power. These flow actuation effects are attributed to gas heating and the resulting dilatational effect on the flow. However, a glow discharge is subject to instabilities especially at high pressures and high current conditions [19]. The effectiveness of a diffuse glow discharge is therefore limited to currents

of a few hundreds of milliamps. At higher currents, the glow transitions to a thermal arc. The arc itself is quite effective in supersonic flow actuation, albeit at much higher power inputs than the glow. For certain conditions, such as those studies by Yano *et al.*, [20] a DC glow discharge in the presence of a supersonic flow did not show any detectable actuation of the flow, reflecting the relatively weak forcing effects that are often realized with plasma actuators in supersonic flows. Flow actuation by large power deposition using filamentary arcs has been explored by Leonov *et al.* [8]. They used an array of small radius electrodes with input currents as high as 1-5A at input voltages of several kilovolts. The power input in these discharges is a few kilowatts and is much higher than in glow discharges. For these arc discharges the static pressure over the wall surface in the immediate vicinity of the discharge was measured and static pressure increases owing to the plasma discharges were found to be insignificant [8]. Similar pressure measurements were conducted by Kimmel *et al.* [5] whose results provide the same conclusions. However, schlieren imaging showed generation of weak shock waves at the location of the arc discharge and the formation of a separation zone immediately downstream of the electrodes [9].

Since non-magnetized DC discharges apparently rely on dilatation effects produced by bulk gas heating, the gas temperature information in the discharge is of great interest. Measurements of the gas temperature using optical emission spectroscopy are common in plasma applications. The Boltzmann plot of spectral line intensities is usually used to find the electronic

temperature. For the estimation of rotational and vibrational temperatures, the spectral line fitting is more commonly used. For air plasma, the rotational bands of N_2^+ first negative system or N_2 second positive system are often used to determine the gas temperature [21]. In an N_2 spectrum, line strengths are usually determined by fitting the measured spectra to synthetic spectra owing to the overlap of rotational lines [21, 22]. For example, Chelouah *et al.* [23] provide a reasonably good estimate of temperature using N_2 and N_2^+ bands by this fitting procedure. Gas temperature measurement in a diffuse glow discharge in supersonic flow has been reported recently by Stanfield *et al.* [24] using nitrogen molecular spectroscopy. They found peak rotational temperatures to be around 380 K at 50 mA current input. A spatial profile of the temperature perpendicular to the surface above the cathode showed that the temperature decreased sharply to near free stream values of about 45 K at an elevation of about 3 mm with the peak occurring just above the cathode. These results indicate that gas heating takes place in only a small portion of the glow plasma volume near the cathode. In a filamentary arc discharge, gas temperatures as high as 3,000 - 5,000 K were measured [9], which is an order of magnitude higher than the case with a diffuse glow discharge [24]. However, as discussed above, flow actuation by arcs is not significantly greater than flow actuation by diffuse glows, despite the much greater power inputs and much higher gas temperatures. Electron number density can be measured using Stark broadening of atomic lines such as hydrogen [25, 26] or helium [27]. Measuring electron number density requires relatively large electron density

($>\sim 10^{14}\text{cm}^{-3}$) [28] for Stark broadening to be significant compared to other broadening mechanisms in the plasma.

Since lower power requirement is critical especially when large area of actuation is required in the current studies, we employ glow discharges rather than thermal arcs. The fact that arc discharge actuation is no better than glow discharge actuation, as shown by previous studies [5, 8], provides additional motivation for the use of glow discharges. Our research will study the coupled interactions between a DC glow plasma discharge, with pin-like electrodes mounted on a surface, and a Mach 2.85 aerodynamic flow. Pin-like electrodes result in abnormal glow discharge operation with higher charge densities and therefore greater discharge intensities. Large area actuation can readily be achieved by using an array of pin-like electrodes, with the total power requirement remaining modest. We seek better understanding of the discharge and its actuation mechanism in supersonic flows.

Flash lamp schlieren and high-speed laser schlieren imaging were used to explore discharge structures and corresponding flow actuation. The emergence of an oblique shock was used as a signature of flow actuation. Electrical measurements, synchronized with imaging, provide a correlation between discharge structure and flow actuation phenomena and time-resolved current-voltage behavior. In order to understand the actuation mechanism, especially the gas heating effect, temperatures in the bulk gas were measured. Non-intrusive optical emission spectroscopy (OES) was used to provide quantitative measurements of the gas temperature, molecular species vibrational temper-

ature, and atomic species electronic temperature. In this work, N_2 and N_2^+ rovibronic bands were used to estimate rotational and vibrational temperature and several Fe (I) atomic lines were used to estimate the electronic temperature. Stark broadening effects were not expected to be significant in these experiments due to the low plasma density (less than 10^{13} cm^{-3}) and hence electron densities were not measured by this approach. Magnetic fields can potentially be applied to increase the effectiveness of plasma discharges by imposing a Lorentz force on the ionized flow. The effect of Lorentz forcing of a supersonic flow by imposed magnetic fields was explored recently, but even in this situation dilatation effects due to gas heating were shown to be the primary mechanism of flow actuation [6]. The effect of a magnetic field on the flow actuation were not also be covered in this study. In addition to gas heating, the effect of electrostatic forcing in DC surface discharges was studied. The effect of electrostatic forcing in supersonic flow actuation is typically assumed negligible by most researchers [29, 30] (one recent exception to this is the paper by Menier *et al.* who addressed the possibility of electrostatic forcing in supersonic flow actuation. [31]). Experimental and analytical approach were made in this study to address a potential role of electrostatic forcing by DC surface discharge actuator.

Chapter 2

Review of related research

In plasma flow control application, the primary objective is to effect gross changes to the flow-field via plasma interaction with the bulk flow. There are many different types of plasma actuators being developed and they utilize different actuation mechanism for flow control. Several representative studies from other researchers will be presented in this chapter.

2.1 Dielectric-barrier discharge flow control

The dielectric barrier discharge (DBD) was developed to generate stable glow discharges at high pressure (one atmosphere) [32]. The dielectric-barrier atmospheric pressure glow (DB-APG) discharge has low current density (of order a few A/m^2) and low temperature (room temperature) characteristics working at a frequency of order a few kHz and at a voltage of several kV [14, 15, 33–35]. Recently, this DBD has been applied in low speed atmospheric pressure flows using a single dielectric-barrier configuration [2, 3, 13]. The driving frequencies and operating voltage are in similar range as DB-APG discharge, which operates up to tens of kHz with up to tens of kV. A major difference from conventional DBD is its configuration where two electrodes of

DBD actuator are placed on the same surface while conventional DBD uses parallel plate electrode-dielectric configuration. One electrode is exposed to the gas while the other is buried under the dielectric to preclude symmetric power deposition during each half cycle [36]. This geometric asymmetry (one bare electrode) results in an asymmetric current waveform, comprising highly pulsed features resulting from filamentation. This asymmetry in current waveform results in the asymmetric forcing. Enloe *et al.* [2] reported that when the exposed electrode becomes negative in potential, the discharge showed more uniform structure and hence produced higher thrust. Note that even though the electrode polarity switches as the voltage waveform oscillates, the effective direction of time-averaged force is always from the exposed electrode to the embedded one [13], which is confirmed by smoke visualization [36]. This indicates that the gas heating effect by DBD can be neglected as a source of the forcing since the dilatation effect produces uniform expansion in all directions.

DBD actuators primarily rely on electro-hydrodynamic (EHD) forcing rather than gas heating. The performance of DBD actuators is evaluated by the magnitude of the induced flow velocity since it directly implies the capability of flow actuation in low speed flow conditions. Roth [3] estimated the induced velocity by assuming that the electrostatic pressure ($\frac{1}{2}\epsilon_o E^2$) is balanced by dynamic pressure ($\frac{1}{2}\rho v_o^2$). The estimation gave an induced flow velocity (v_o) of order 10 m/s. In the paper, the author also reported that using a so-called peristaltic flow acceleration mechanism the induced neutral gas velocity can become as large as 100 m/s assuming ion drift velocity is equal

to induced neutral convection velocity. This becomes realistic only when the ion number density increases significantly. In practice, however, the peristaltic flow actuation achieves flow velocity of only several m/s. Leonov *et al.* [9] gave a similar estimation of induced speed as high as about 10 m/s by equating electrostatic force (qE) with an acceleration of a neutral gas ($\dot{m}$V). They commented that in a real physical situation, a significant improvement in induced speed greater than the above estimate is not possible because a continuous increase of current leads to energy deposition to thermal modes by heating the gas and surface. A numerical study [13] supports the above estimates, in which the maximum flow speed induced by a plasma was no more than 6 times the 2 m/s free stream velocity. At higher free stream velocity, the actuation was less than twice the free stream velocity, which means the induced flow velocity was lower than the 10 m/s suggested above. Even though the actuation effect is rather modest, DBD flow actuator has gained increasing interest recently. In fact, several m/s actuation can be sufficient in low speed flow conditions. Roth demonstrated the plasma induced flow re-attachment with dielectric barrier on an airfoil [3]. Similar work has been done by Post *et al.* on flow separation control [37] showing the lift enhancement by plasma actuator. Flow separation control technique was applied recently to a low pressure turbine blade [38]. Plasma synthetic jets have also been tested by using a circular DBD configuration [4, 39]. DBD actuators have been only applied to low speed flows partly because the expose electrode interferes with supersonic flow and partly due to low induced flow velocity.

2.2 DC-discharge flow control

Another type of discharge that is used in flow actuation is the DC discharge. Early experiments on DC plasma flow actuation were a thruster called 'Ionocraft' which used a corona discharge [40]. A corona discharge occurs when one of the electrodes has small radius of curvature so that the local high electric field accelerates background electrons and produces a so called 'ion wind' [41]. The positive ions drifting in the collection (cathode) area of the corona away from the high field near wire/point region are the main cause for actuation. One of most common uses of corona discharge is a generation of ozone [42]. Recently, corona discharges are being investigated again in the area of flow actuation [43].

In high speed flows, high current DC discharges are used. In a DC discharge at supersonic flows, input voltages of up to ∼10 kV are applied with a current of about 10's mA - several A. Electrodes are flush-mounted onto the actuator surface which is made out of dielectric refractory materials. The anode and cathode can be co-planar or placed on different surfaces. Electrode arrangement, size, number of electrodes and polarity can vary depending on the desired output performance. The plasma discharge mode can be established as a glow [5, 6, 20, 44] or filamentary arc [8, 9]. These two types of plasmas are obtained in different power regimes. Glow discharge occurs at lower currents with high plasma resistance whereas an arc tends to form when the input current increases significantly (∼1 A).

Yano *et al.* used a DC discharge at the nozzle inlet section of a super-

sonic wind tunnel to generate a volumetric ionized flow in the test section [20]. DC discharge in the nozzle inlet also provided a means to visualize the flow in the test section. But owing to a low actuation effect achieved by low ionization fraction ($n_e/n_g \sim 10^{-9}$) they could not detect any measurable shock modification by this DC plasma.

Kimmel *et al.* used a single pair of relatively large size electrodes to produce a glow discharge with an input power of ∼10's W [6]. A large volume diffuse discharge formed above the cathode in a Mach 5 flow. They explored streamwise and cross-flow arrangement of electrodes and the maximum effect was obtained from the streamwise discharge with cathode upstream [5]. They reported that in streamwise electrode arrangement with cathode located upstream, the surface pressure increment (about 10 %) caused by plasma was observed immediately after the cathode and varied roughly linearly with applied input power. Peak electron number density of 10^{12} cm^{-3} was measured above the cathode using a double Langmuir probe [6]. In recent work on temperature measurement using emission spectroscopy [24], the peak rotational temperature was about 380 K for a 50 mA current input. The temperature profile showed that above the cathode, the temperature sharply decreased to near free stream temperature (about 45 K) at around 3 mm distance from the cathode surface plane and the peak occurred right above the cathode. It was seen from the temperature profile above cathode that the gas heating was achieved only over a small portion of the plasma volume. But above the anode, the temperature remained constant at around 295 K up to 3 mm elevation. In

a study of lift force [18] using a laser displacement sensor, the maximum lift force on a 5.1 cm×3.8 cm actuator plate was measured at one gram for a 24 mA current input. The lift force was linear with the input power. However, glow discharge is quite unstable especially at higher power [19]. Hence the effect of diffuse glow discharge including the linearity on lift force no longer holds at higher currents and the operating current input is limited to a few hundred mA.

Since Joule heating by DC surface discharge is significant and is an important actuation mechanism in supersonic flow control, an arc discharge is desirable due to the capability of a higher power loading. Leonov *et al.* [8] used an array of small radius electrodes with significant power input. The input current was as high as 1-5 A at an input voltage of several kV resulting in total power of several kW. The discharge in turn formed a filamentary arc. The increase of a static pressure produced by the filamentary arc discharge was no greater than that of glow discharges mentioned above. However, schlieren imaging showed the generation of an oblique shock by forming a separation zone of hot air downstream of electrodes to deflect streamlines [9]. Navier-Stokes simulations using a $k-\omega$ turbulence model for the same experimental configuration showed a large region of subsonic flow downstream of the cathode, which demonstrates the existence of plasma induced shock [9]. Gas temperatures were measured as high as 3,000 - 5,000 K using a spectroscopic technique, which is an order of magnitude higher than the case with a glow discharge introduced in the previous paragraph. The interaction of an induced

shock with existing flow field using a filamentary arc was shown to be significant so that the reflected shock angle increased in the presence of a surface discharge resulting in a stagnation pressure drop by 5%.

2.3 RF-discharge flow control

Whereas a DC glow discharge is subject to strong instabilities, an RF discharge can generate a stable glow discharge at relatively higher current. Merriman *et al.* [12] developed a wind tunnel with DC discharge at the nozzle inlet and an RF discharge in the test section. The RF discharge increased the electron number density in the test section and generated a higher density plasma with increased ionization fraction ($n_e/n_g \sim 10^{-8}$-10^{-6}). Although their previous setup which had only the DC discharge could not provide any visible flow actuation, they were able to show shock angle modification by the ionized flow (from 99 to 113 degree) using this new setup with an RF discharge. The time scale to modify the shock angle was a few seconds compared to the flow residence time scale of the order 10 μsec, which implies the actuation mechanism is purely a thermal heating effect produced by the plasma. It must be noted that the main advantage of using an RF discharge for a flow actuation is the ability to alter the flow field in the full test section volume and to generate more conductive flow to increase the interaction with an external magnetic field. To provide a localized actuation in supersonic flows, a surface DC discharge or thermal arc are preferred.

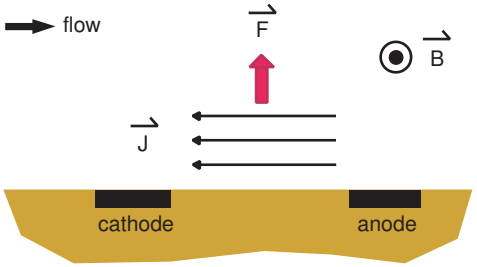

Figure 2.1: Lorentz force produced in the presence of external magnetic field.

2.4 Magnetohydrodynamic (MHD) flow control

The improvement of plasma flow actuation can be achieved by applying an external magnetic field to an ionized flow. The additional forcing on the flow by a magnetic field is produced by a Lorentz force ($\overrightarrow{J} \times \overrightarrow{B}$) in addition to Joule heating ($\overrightarrow{J} \cdot \overrightarrow{E}$). To produce a significant effect of the magnetic field, the interaction parameter (Stuart number, $I = \frac{\sigma B^2 L}{\rho u}$) has to be $O(1)$ or higher than unity [45].

Menart *et al.* [5] reported that the surface pressure was altered by Lorentz force produced by the external magnetic field as illustrated in Fig. 2.1. However, a reversal in the polarity of the magnetic field which in turn is supposed to change the direction of Lorentz force showed the same effect of increasing surface pressure. This was not an expected result since the opposite forcing should decrease the pressure by flattening the boundary layer. They conjectured that the main mechanism for actuation was still Joule heating even in the presence of the magnetic field. Joule heating is independent of the direction of the magnetic field. A later paper by Kimmel *et al.* confirmed that the magnetic field effect was not very promising [6]. Surface pressure

increase by the plasma was maximum when no magnetic field was applied. In the presence of a magnetic field with resultant Lorentz force in normal upward or downward direction of actuator plate, the pressure increase was suppressed. Note that the pressure increase can be controlled by changing current alone in the absence of external magnetic field. If the applied magnetic field cannot increase the surface pressure higher than the pressure increase owing to changing current alone, there is no need for magnetic field. However, Leonov *et al.* [8] demonstrated that the magnetic field can modify the oblique shock position and angle in a way that the effect of the magnetic field was in addition to the effect of current input resulting in a bigger actuation. They noted in a later paper [46] that the effect of magnetic field was not large and proposed a bottom-to-top direction of magnetic field with transverse electric field. In that paper, it was shown that the Lorentz force due to the magnetic field (B=1.2 T) directed upstream of the flow can hold the filamentary discharge between electrodes, otherwise the discharge column is stretched downstream away from the electrodes in the absence of the magnetic field.

Meyer *et al.* [45] reported an MHD effect on turbulent boundary layers claiming that the interaction parameter can be effective in turbulent boundary layers at relatively low plasma conductivities typical of glow plasmas. Using laser-differential-interferometry (LDI), the frequency spectrum of density fluctuations was measured in the presence of an external magnetic field. Their results showed that a decelerating Lorentz force amplified turbulent fluctuation intensity (about 10-20%) while an accelerating force reduced them. The

effect was bigger with increasing flow conductivity, which was achieved by increasing RF power. Note that the effect of external magnetic field provides a body force in addition to EHD force and/or gas heating effect.

Chapter 3

Experiment setup

3.1 Wind tunnel

The supersonic flow plasma actuation experiment work was conducted in a Mach 2.85 wind tunnel located at the Pickle Research Center at the University of Texas at Austin. The overall schematic of wind tunnel facilities is shown in Fig. 3.1. The tunnel is fed by a 500 ft^3 high-pressure tank and the air is discharged into a 1000 ft^3 vacuum tank. The vacuum tank is evacuated to a pressure of 5 - 10 Torr using a Stokes micro vacuum pump (Model: 412H-11) and Roots Connersville rotary positive vacuum pump (RGS-HVB). The stagnation pressure and test section pressure is monitored by pressure transducers inserted in desired places. The test section pressure is maintained in the range of 15 to 25 Torr for all experimental runs by adjusting stagnation pressure. The free stream static temperature is expected to be about 110 K and free stream Reynolds number is about 500,000 - 1,000,000. The run time of wind tunnel is less than about one minute. The vacuum pump requires at least a 15 minute pause before a restart to avoid overheating.

Figure 3.2 illustrates the schematic of wind tunnel with actuator plate placed inside the test section. The wind tunnel has a 5 cm$\times$5 cm test section

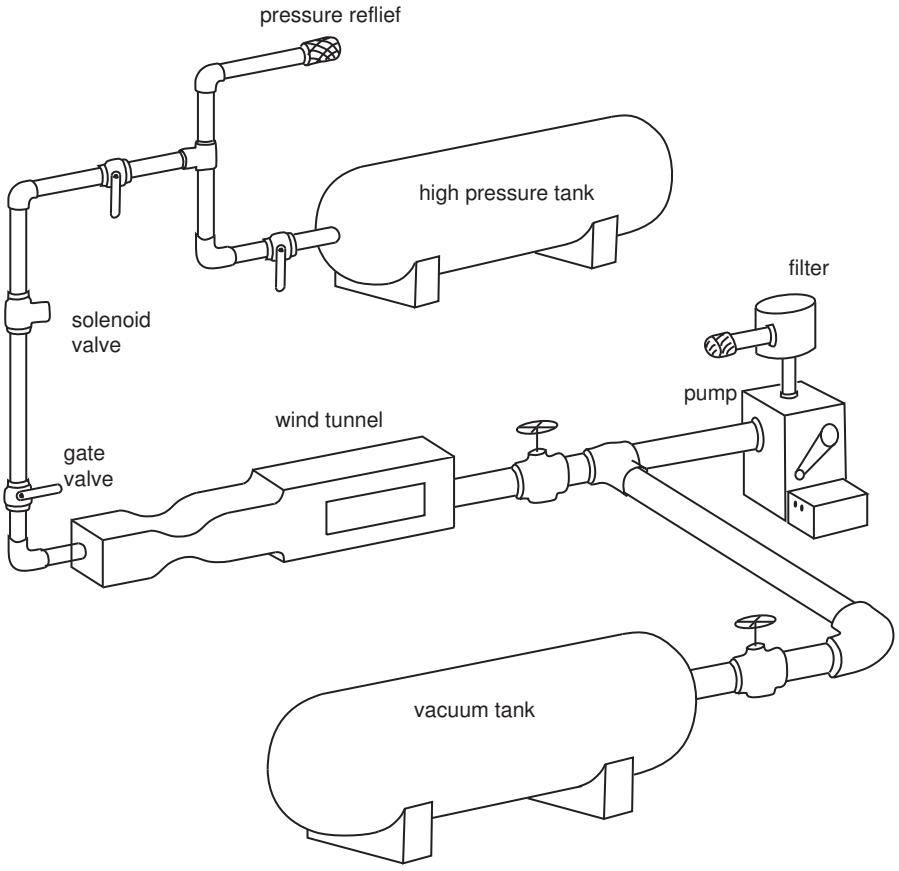

Figure 3.1: Overall schematic of wind tunnel facilities located at the Pickle Research Center at the University of Texas at Austin.

and is equipped with adjustable upper and lower test section walls, which enable the mean pressure gradient to be set. Fused silica view windows of 2 inch$\times$ 8 inch were located on each side of test section and a 1 inch$\times$ 5 inch fused silica view window was located on the top of test section. An acrylic splitter plate with 6.0 mm thickness was inserted which extended from the plenum section to the test section. The plasma actuator was installed at the tail of splitter plate as shown in Fig. 3.2 and the electrodes were located about 4.5

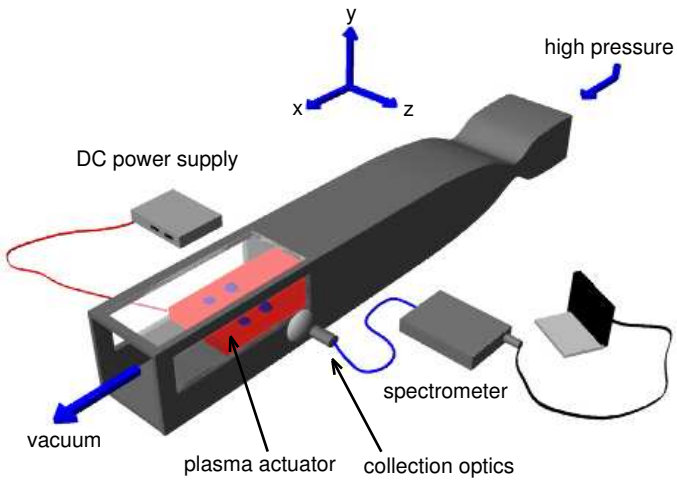

Figure 3.2: Schematic of experiment setup of wind tunnel for the study of supersonic flow actuation by direct-current surface discharge plasma.

inches downstream from leading point of the test section. Details of the plasma actuator will be presented in the following section. A plastic splitter plate was used to avoid any secondary discharges that could form between electrodes and a metal splitter plate. For the same reason, the inner wall of wind tunnel was insulated with Kapton tape. In the event of secondary discharge, the main discharge on the actuator fails to turn on. Due to flexibility of the plastic splitter plate, the tail of actuator needed to be firmly held from the wall on each side of test section to avoid vibration of splitter plate caused by supersonic flow. Additional details on the wind tunnel can be found in Ref. [47].

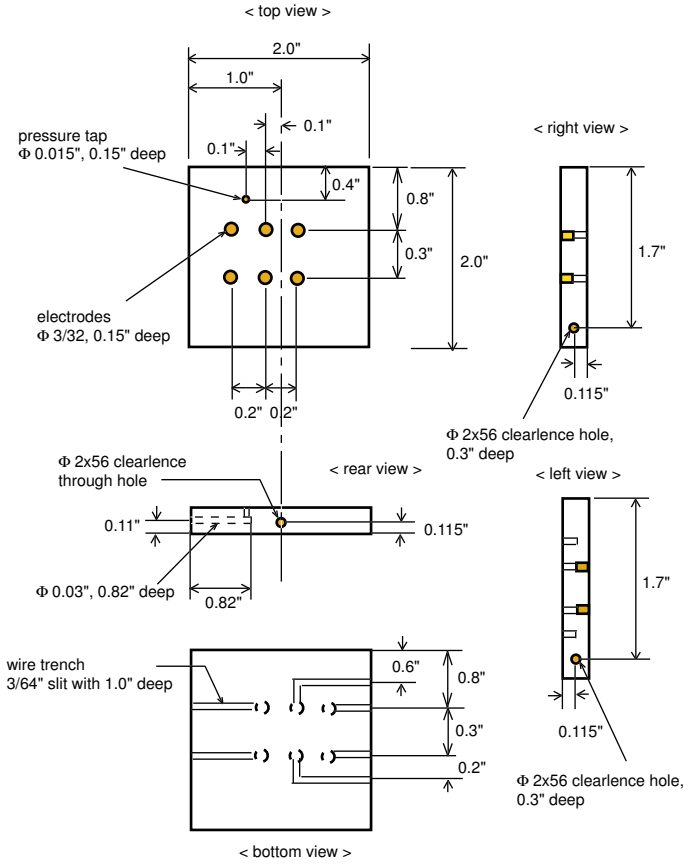

Figure 3.3: Electrode arrangement for supersonic flow plasma actuator with an array of steel pin electrodes of diameter 3/32 inch.

3.2 Plasma actuator

An actuator dielectric block was inserted at the tail of center plate and was made out of ceramic material (Macor^{TM} or Resco^{TM}) to withstand high temperature due to significant surface heating by the plasma. This material can stand up to 3000^{o}F and the melting point is about 3400^{o}F. A detailed drawing of the actuator block is shown in Fig. 3.3. Pin-like steel electrodes (dia.

3/32 inch) are flush-mounted on actuator plate so that electrodes themselves do not perturb the supersonic flow. A steel rod for electrodes was cut into several pieces about 0.2 inch in height. A 0.013 inch hole was drilled to about 0.08 inch depth at the center of one end of each electrode. An electrical wire was inserted into the hole and then the electrode was crimped to hold the wire. The electrodes with wires connected to them were then inserted from the top surface of actuator block with wires coming out of the bottom surface and were forced down to fit into a 3/32 inch dia. dip in the actuator dielectric block. Once all the electrodes were tightly fit into each hole, the top surface was milled down by about 1/100 of inches to make an actuator surface flush with the dielectric surface. Wires that were pulled out on the other side were then bent to sit into each slit in the dielectric block so that they are not exposed to a supersonic flow on the bottom side of actuator plate. A thin layer (about 1 mm) of insulating paste (cold weld) was applied along slits on the bottom side to protect wires and to prevent parasitic discharge between wires.

The electrodes were oriented in the stream-wise direction with one electrode upstream and the other downstream of it. The inter-electrode distance measured between electrode centers was 0.3 inches. Previous work by Menart *et al.* [5] showed that the actuation was more effective when the electrodes were arranged in the stream-wise direction with the cathode located upstream. Both cathode downstream and cathode upstream configurations were considered in this study to explore the effect of cathode location on flow actuation. Figure 3.4 shows an image of the actuator plate installed inside the wind tunnel.

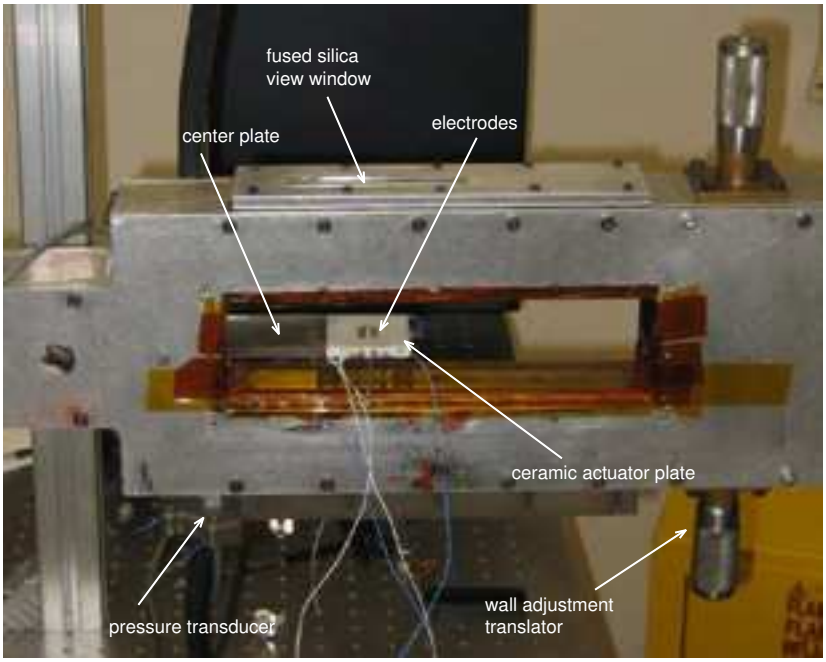

Figure 3.4: Plasma actuator installed inside wind tunnel.

The discharge power was provided by a 1.2 kW high-voltage, high-current DC power supply (Spellman, SL2PN1200), which is rated to deliver a maximum current of 600 mA and a maximum voltage of 2 kV. Figure 3.5 shows a detailed electric circuit diagram of the plasma actuator. Variable ballast resistors (R_1, R_2 and R_3) whose resistance ranges from 0 to 25 kΩ were connected in series to each cathode to control the discharge operating regime. Typical value of ballast resistance was about 1 - 5 kΩ. To accommodate the high power loading of the ballast resistor, 225 W resistors (Ohmite, D225k25k) were used. To avoid significant power loading through ballast resistors, more

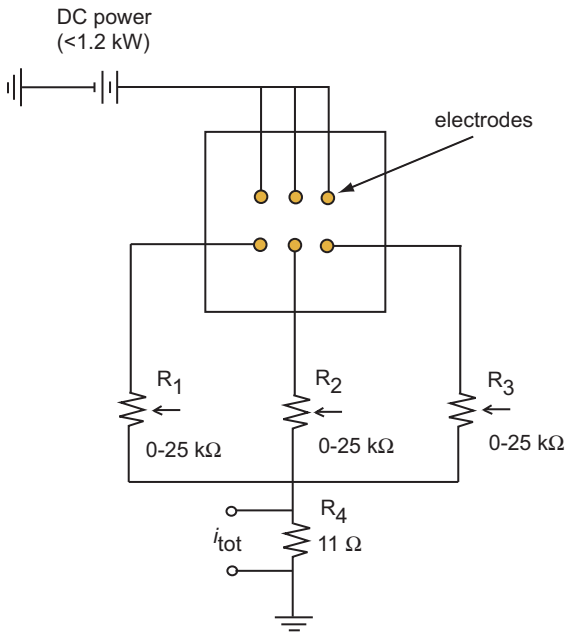

Figure 3.5: Detailed electric circuit diagram of the plasma actuator.

than one resistor could be connected in parallel so that the current through each resistor could be lowered. When an array of discharge was used, individual ballast resistors through each discharge pair needed to be adjusted so that all desired pairs could form discharges at the same time. The total discharge current was measured by measuring the voltage drop across a 11Ω resistor (R_4) connected in series to the discharge downstream of ballast resistors and was recorded using a data acquisition card (DAQcardTM-AI-16E-4). The transient discharge current measurement was synchronized with the high-speed laser schlieren imaging system. Wind tunnel and optical table were properly grounded and live wires were properly insulated to avoid a short.

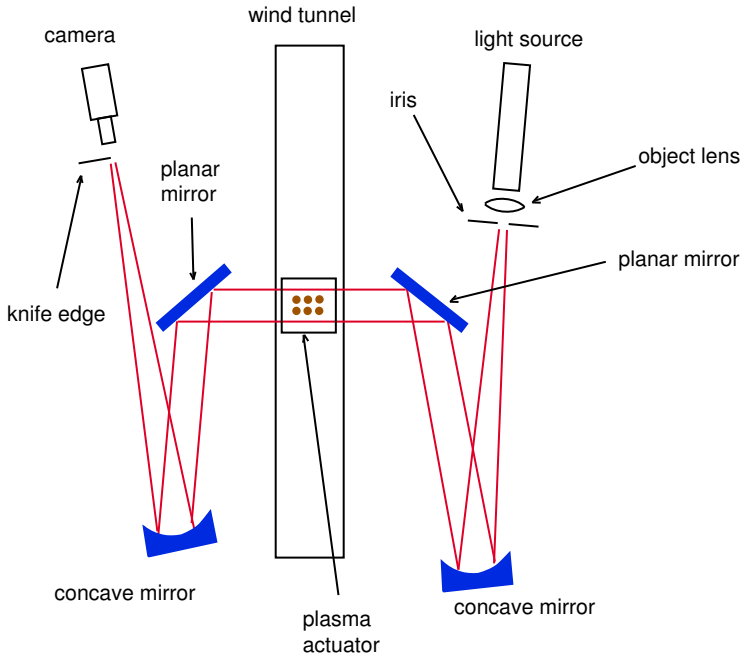

Figure 3.6: A schematic of schlieren imaging system. Both flash lamp schlieren and laser schlieren use the same setup except light source and camera are replaced correspondingly.

3.3 Schlieren imaging

Flash lamp schlieren imaging and laser schlieren imaging were used in this study to visualize the flow field structure in a supersonic flow. Figure 3.6 shows a schematic of schlieren imaging system. The flash lamp was pulsed at 60 Hz using a BNC delay generator. The flow was imaged through side view windows on each side of the test section. The light passed through an iris in front of flash lamp and expanded on to 3 ft. focal length concave mirror. Collimated light from concave mirror passed through actuator plate and was focused by another 3 ft. focal length concave mirror. Care was taken to ensure

that the line-of-sight imaging by camera and collimated light path were parallel to actuator plate as shown in Fig. 3.6. Horizontal knife edge was placed in the focal plane to cut off aberrated light and increase sensitivity of schlieren image. The flash lamp schlieren images were captured using a Pulnix TM 6710 camera with a framing rate of 60 Hz, triggered internally, and had an exposure time of 16 ms. The images (512×480 pixel resolution) were acquired for 30 seconds once the tunnel was started. For a high speed schlieren imaging, light source and camera were replaced with a steady-state helium-neon laser (5 mW) and a high-framing rate CCD camera (Kodak Ektapro 4540mx), respectively. A laser beam was focused by 5 mm focal length object lens and passed through 25μm pin hole. The pin hole blocked out higher frequency diffraction pattern and provided homogenous laser beam. Diffraction fringes caused by knife edge were not avoidable and could be removed to some extent by post filtering of images using a Matlab program. The resolution of the CCD camera was 256×256 pixels and the framing rate was 4.5 kHz. The pulse duration of about 222 μs was small enough to provide an instantaneous snapshot of the flow structure. The start of the image acquisition was controlled using a BNC delay generator and the images were acquired with an internal trigger. Images were low pass filtered to remove video noise.

3.4 Spectroscopy

Optical Emission Spectroscopy was used in this study to obtain gas and electronic temperature information in the discharge. The light emitted

from the discharge was collected with a 1 inch focal length confocal lens (dia. 1 inch) through a fused-silica side window and was focused on to a fiber optic cable with a 400 μm core. The fiber optic and collection lens were mounted on the x-y translation stage to provide spatial profile of emission spectra. The fiber optic was connected to the entrance slit (5 μm slit width) of a 1/4 m imaging spectrometer (Spectra-Physics, MS260i). The nominal spectral resolution of the spectrometer was 0.13 nm with a 1800 lines/mm grating. Gated linear CCD detector (Oriel Linespec^{TM}) has 200 μm (H)$\times$ 7 μm (W) pixel size. The spatial resolution of the optical setup was measured by translating the optics (fiber optic and lens) horizontally across a 25 μm pin hole which was back-illuminated by a flash lamp on the object plane. The spatial resolution was found to be limited by the fiber optic cable core diameter and the magnification of the system (i.e. resolution = dia./magnification). Figure 3.7 shows a measured spectral intensity profile of the pin hole point light source. Spatial resolution was shown to be about 400 μm FWHM, which was the same as the fiber optic core diameter. Spectral line positions were calibrated using a Mercury lamp. All measurements were done in a dark room and background spectrum was subtracted from each measured spectrum. Depending on the intensity of emission spectra, integration time was adjusted such that line fitting for temperature estimation was possible. At least two data sets were averaged to reduce a noise at every measurement point. Molecular spectroscopy and temperature estimation will be discussed in Ch. 4.

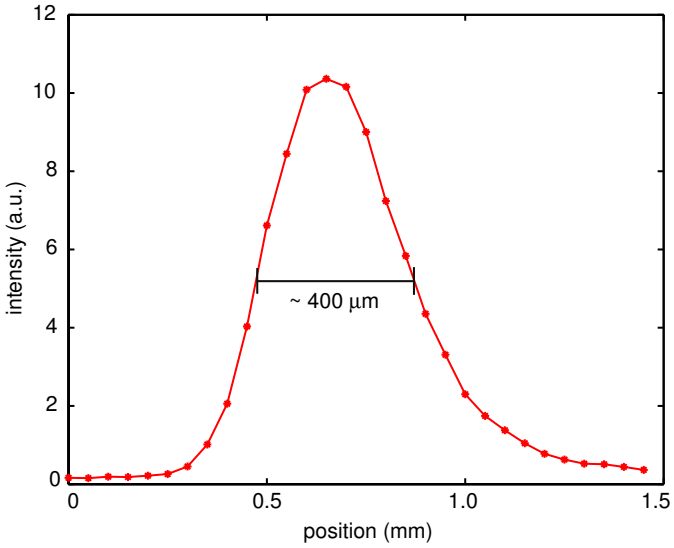

Figure 3.7: Spectral intensity profile obtained by translating the collection optics across the point light source. The spatial resolution (FWHM) was about 400 μm.

3.5 Planar Laser Mie Scattering and Particle Image Velocimetry

A separate experimental setup shown in Fig. 3.8 was used to study the effect of electrostatic force by a DC surface discharge. Since it was hard to explore the EHD forcing effect experimentally in a supersonic flow, a stagnant chamber was used to visualize induced flow field produced by DC surface discharge. In this study, planar laser Mie scattering (PLMS) and 10 Hz particle image velocimetry (PIV) were used. The plastic chamber was a 9"x7"x3" and was able to provide a pressure as low as 1 Torr. The chamber was evacuated using mechanical pump (Edwards, RV-8). Seed particles were delivered into the chamber through 1/4 inch tube by a pressure gradient between the evac-

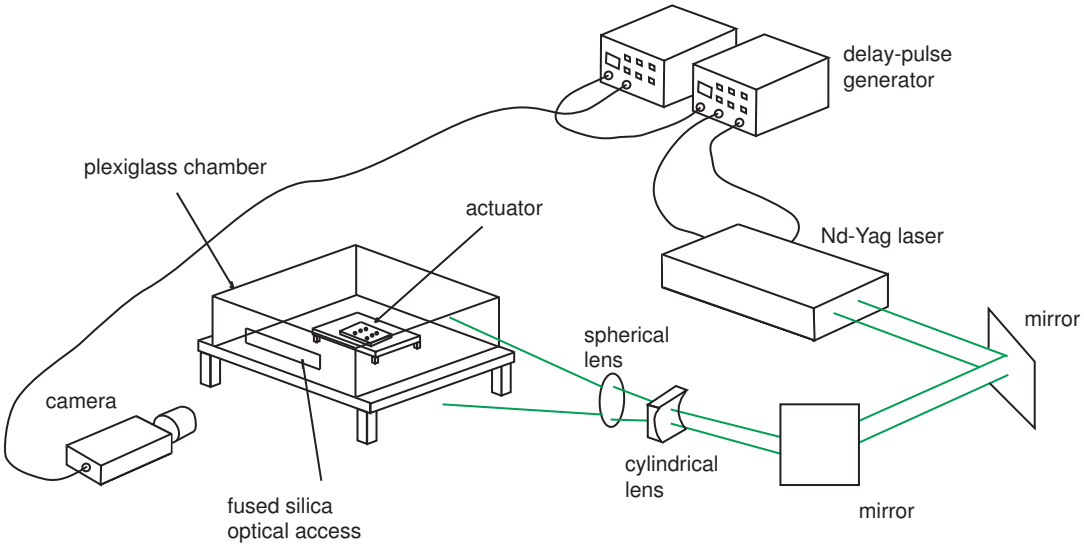

Figure 3.8: Experiment setup for PLMS and PIV study of induced flow field.

uated chamber and ambient air. Both PLMS and PIV techniques require a uniform seeding of sub-micron size particles. Glycerin, alumina (Al_2O_3) or TiO_2 seed particles were used in this study. Glycerin particles were generated by a fog machine (Rosco 1600) and stored in a small paper box to form a denser fog and then added into chamber. The solid particles (Alumina and TiO_2) were baked (heated at 350^{o}C) before feeding into a chamber to remove a water vapor in the particles and to avoid agglomeration of particles. To minimize agglomeration of solid particles, a cyclotron seeder could be used to dispel heavier (agglomerated) particle and to feed only lighter particles into a chamber. In this study, cyclotron seeder was not used. Due to the contamination of chamber and especially the optical window by seed particles, regular cleaning was needed after 2-3 experimental runs.

An Nd-Yag laser (PIV-400) was used to illuminate seed particles. It generates dual green laser beams (532 nm wavelength) by frequency-doubling a 1064 nm beam. The time between the two laser beams was adjusted by using a pulse-delay generator (SRS DG535) depending on the estimated flow velocity. If the time delay is too short compared to flow time scale, the two images will look identical. If the time delay is too large, the particle movement cannot be determined. Also two beams should have the same power so that the luminosity of both images becomes equivalent to provide correct correlation. Laser light was collected through mirrors and focused on the actuator plate by 350 mm plano-convex lens. The cylindrical lens expanded the laser beam to produce a planar laser sheet across actuator plate. Two planar laser sheets must coincide with each other so that they hit the same image plane, otherwise two frames may image different particles on different image plane and the correlation between two frames fails. Flow field images were taken by a CCD camera (Kodak Megaplus ES1.0) which was triggered by a digital pulse-delay generator (SRS DG353). The image size was 1024×1024 pixels. To minimize luminosity from the plasmas, Ferroelectric Liquid Crystal (FLC) shutter was mounted between the camera and camera lens. The exposure time of the FLC shutter was about 200μsec. Details regarding PIV measurement can be found in Ref. [48]

Chapter 4

Optical emission spectroscopy

4.1 Introduction

Important part of this study is to characterize correct temperatures in the discharge using optical emission spectroscopy. This chapter will discuss about molecular spectra which are essential to estimate temperatures. Typically molecular spectra are much more complex than atomic spectra due to the complex structure of molecules. One important application of molecular spectroscopy is an estimation of the rotational and vibrational temperature of molecular gases based on the fact that the population of rotational and vibrational states are a function of rotational and vibrational temperature, respectively. In aerodynamic applications such as in this study, the working gas is primarily air. Because it is the principal component in air, nitrogen molecular spectroscopy is often used. Furthermore, nitrogen spectra can be easily identified in nitrogen carrying plasmas [49] and extensive reference data are available in the literature [21, 50–53]. Hence molecular spectroscopy focusing on nitrogen spectra will be discussed in this chapter. A corresponding temperature measurement in a supersonic flow will be presented in Ch. 6.

The molecular electronic state is designated as Σ,Π,Δ,Φ,$\cdots$ depending

on $\Lambda = 0, 1, 2, 3, \cdots$ where Λ is a quantum number denoting the projection of the angular momentum of the electrons along the internuclear axis. The angular momentum of molecules including electrons is modelled using vector diagram. For the symmetric top model, vector $N(= 0, 1, 2, \cdots)$ describes the angular momentum of nuclear rotation which occurs at right angles to the internuclear axis. This represents the rotation of nuclei and does not contain the nuclear spin angular momentum. The nuclear spin is responsible for the hyperfine structure in line spectra and the intensity alternation in band spectra (Ref. [54], p.29). Total angular momentum $J = \Lambda + N$. When $\Lambda = 0$, $J = N$ and structure is explained by simple rigid body rotator model since the term including Λ in rotational energy vanishes which makes the rotational term equal to that of simple rigid rotator.

Detailed expressions for the energy levels of molecules can be determined when the influence of rotation, vibration and electronic motion on each other is defined. Interaction between rotation and vibration is considered in the rotational energy term where rotational constants are a function of vibrational quantum number. Interaction between vibration and electronic motion is represented in the potential curve which includes the dependence of the electronic energy. The influence of rotational and electronic motions on each other is modelled by Hund's coupling cases. In Hund's case (a), electronic motion is strongly coupled to the internuclear axis. Hence, total electronic angular momentum that describes the projection of total angular momentum J to internuclear axis becomes $\Omega = |\Lambda + \Sigma|$ instead of Λ in symmetric top

model given above. Σ represents the projection of electron spin vector S on to internuclear axis and hence can be expressed as the coupling of electron spin with the internuclear axis. Here, $\Sigma(= S, S-1, \cdots, -S)$ represents a quantum number for electron spin for molecules and differs from Σ describing the molecular state ($\Lambda = 0$) presented above. In Hund's case (b), spin vector S is not coupled to the internuclear axis. When $\Lambda = 0$ and $S \neq 0$, Ω is not defined and hence case (a) cannot describe this decoupling effect. In Hund's case (b), quantum number $K = \Lambda + N$ is designated which represents total angular momentum apart from spin and $J = K + S, K + S - 1, \cdots, |K - S|$ describes total angular momentum including spin. Detailed explanations about Hund's coupling cases can be found in Ch. V of Ref. [54].

Rotational levels are called either positive or negative. Positive means the total eigenfunction ($\psi = \psi_e \frac{1}{r} \psi_v \psi_r$, Ref. [54], p.129) remains unchanged for a reflection at the origin. For a Σ state ($\Lambda = 0$), rotational levels start with positive or negative depending on whether electronic eigenfunction (ψ_e) remains unchanged (Σ^+) or changes (Σ^-) with respect to the reflection to the axis of symmetry. If $\Lambda \neq 0$, rotational levels always start with positive and change signs at every rotational line. When $\Lambda \neq 0$, a structure is a symmetric top and each J has both positive and negative levels with the same energy because the rotational energy of symmetric top is doubly degenerate upon the reflection of nuclei along N. For further details about symmetry properties, refer to the Ch.III, Sec.2(f) of Ref. [54]. Once the detailed energy level is defined by appropriate quantum numbers, the transition between two levels

is determined by selection rules which are obtained by evaluating the matrix elements of the electric dipole moment.

4.2 Emission spectral line intensity

Predicting accurate emission line intensity of atoms or molecules is important when one wants to make temperature measurement of plasmas. In this section, a complete description of emission line intensity will be provided. The reader is encouraged to refer to [54–56] for details.

Emission from plasma is due to the energy release of photons that are produced by de-excitation of species in a given energy state. The energy that is released by single photon is $E[J] = h\nu$, where $h = 6.626068\times\ 10^{-34}$ $[J \cdot s]$ is Planck constant, and ν [1/s] is a frequency of emitted photon. The emission intensity can be expressed as (Ref. [54], p.20)

$$I_{em} = N^{'} h\nu_{''}^{'} A_{''}^{'}, \tag{4.1}$$

where $N^{'}$ is a number density of upper state (or number of atoms/molecules), $\nu_{''}^{'}$ is a transition frequency and $A_{''}^{'}$ is an Einstein coefficient that describes a transition probability of spontaneous emission. Conventionally, $^{'}$ represents an upper state and $^{''}$ represents a lower state. In order to estimate emission intensity accurately, one must use correct values for the transition probabilities of electronic-vibrational transitions.

The Einstein coefficient, $A_{''}^{'}$ is related to electronic-vibrational transi-

tion moment, $(R_{''}^{'})^2$ as follows [57]:

$$A_{''}^{'} = \frac{64\pi^4\nu^3}{3h}\frac{(2-\delta_{0,\Lambda^{'}+\Lambda^{''}})}{(2-\delta_{0,\Lambda^{'}})}\left(R_{''}^{'}\right)^2 \tag{4.2}$$

$$\left(R_{''}^{'}\right)^2 = \left(\int \Psi^{'} R_e(r) \Psi^{''} dr\right)^2, \tag{4.3}$$

where

$$\begin{cases} \delta & \ldots \text{ Kronecker delta} \\ r & \ldots \text{ internuclear distance} \\ \Psi^{'}, \Psi^{''} & \ldots \text{ vibrational wave function of upper and lower state, respectively} \\ R_e(r) & \ldots \text{ electronic transition moment function (ETMF).} \end{cases}$$

When ETMF varies slowly with the internuclear distance, r , Eq. 4.3 can be approximated as (Ref. [54], p.200)

$$(R_{''}^{'})^2 \cong (R_e(\bar{r}))^2 \left[\int \Psi^{'}\Psi^{''} dr\right]^2. \tag{4.4}$$

Here, $\left[\int \Psi^{'}\Psi^{''} dr\right]^2$ is called the Franck-Condon factor ($\equiv q_{''}^{'}$) that determines the intensity of vibrational transitions for given electronic transition and the integral is called the vibrational *overlap* integral. Combining Eqs. 4.2 and 4.4 gives the complete form of the Einstein coefficient as

$$A_{''}^{'} = \frac{64\pi^4\nu^3}{3h}\frac{(2-\delta_{0,\Lambda^{'}+\Lambda^{''}})}{(2-\delta_{0,\Lambda^{'}})}(R_e(\bar{r}))^2 q_{v^{'}v^{''}}. \tag{4.5}$$

The term *oscillator strength* ($\equiv f_{v^{'}v^{''}}$, Ref. [52])

$$f_{v^{'}v^{''}} = \frac{8\pi^2 mc\nu}{3he^2}\frac{(2-\delta_{0,\Lambda^{'}+\Lambda^{''}})}{(2-\delta_{0,\Lambda^{'}})}(R_e(\bar{r}))^2 q_{v^{'}v^{''}} \tag{4.6}$$

is often used to describe the radiation process and customarily used in absorption process [58]. When all rotational transitions between a given $J^{'}$ and all

possible $J^{''}$ are summed up,

$$\Sigma(R_e)^2 q_{v^{'}v^{''}} = (2 - \delta_{0,\Lambda^{'}+\Lambda^{''}})(2S^{'}+1)(R_e)^2 q_{v^{'}v^{''}}.$$

This is also called *band strength* of electronic-vibrational transition and often named as $S_{v^{'}v^{''}}$. $2S^{'}+1$ is a spin multiplicity. Using $S_{v^{'}v^{''}}$, Einstein coefficient can be rewritten as follows:

$$A_{''}^{'} = \frac{64\pi^4\nu^3}{3h}\frac{S_{v^{'}v^{''}}}{(2-\delta_{0,\Lambda^{'}})(2S^{'}+1)}. \tag{4.7}$$

From Eqs. 4.1 and 4.7, the emission line intensity is represented as

$$I_{em} = \frac{64\pi^4}{3h}\frac{N^{'}h\nu_{''}^{'4}}{(2-\delta_{0,\Lambda^{'}})(2S^{'}+1)}S_{v^{'}v^{''}}. \tag{4.8}$$

The population in the upper state is now described by Boltzmann distribution for corresponding electronic, vibrational and rotational temperature. Populations of upper electronic, vibrational and rotational state are [51],

$$N_{n^{'}} = \frac{N_o}{Q_{el}}(2-\delta_{0,\Lambda^{'}})(2S^{'}+1)\exp^{-E_{e}^{'}/kT_e} \tag{4.9a}$$

$$N_{n^{'}v^{'}} = \frac{N_{n^{'}}}{Q_v}\exp^{-E_{v}^{'}/kT_v} \tag{4.9b}$$

$$N_{n^{'}v^{'}J^{'}} = \frac{N_{n^{'}v^{'}}}{Q_r}g_{J^{'}}\Phi_{P^{'}}\exp^{-E_{r}^{'}/kT_r}. \tag{4.9c}$$

where

N_o, $N_{n^{'}}$, $N_{n^{'}v^{'}}$, $N_{n^{'}v^{'}J^{'}}$	total number density, number density of electronic, vibrational and rotational state, respectively.
$E_e^{'}$, $E_v^{'}$, $E_r^{'}$	energies in electronic, vibrational and rotational states
T_e, T_v, T_r	electronic, vibrational and rotational temperature
Q_{el}, Q_v, Q_r	partition function of electronic, vibrational and rotational state
$g_{J^{'}}$	degeneracy of rotational state
$\Phi_{P^{'}}$	takes care of intensity alteration of rotational lines.

With Eqs. 4.8 and 4.9, the emission line intensity for any transitions can be obtained. The usage of these equations will be covered in the following sections and Sec. 6.1. Note that $g_{J'}$ is equal to $2J^{'}+1$ but in Hund's coupling cases which will be covered in the next section, various formulae for line strength are possible depending on the rotational transitions. However, the summation for the same $J^{'}$ of these formulae turns to be equal to $2J^{'}+1$. This will be shown in the following sections where rotational levels of N_2 and N_2^+ system are introduced. If the two states (upper and lower states) are described by one of Hund's coupling cases, the line strength is also called the Hönl-London factor [54]. Extensive study on Hönl-London factor of diatomic molecules can be found in ref [59].

4.3 N_2^+ spectra

A first negative system (FNS) of N_2^+ band spectra at 391.44 nm and 427.81 nm represents a transition between $B^2\Sigma_u^+$ and $X^2\Sigma_g^+$. $^2\Sigma$ states strictly follow Hund's coupling case (b). The selection rules that apply for this case are summarized below.

1. $\Delta J = 0, \pm 1$, but $J = 0 \nleftrightarrow J = 0$
2. $+ \leftrightarrow -$, $+ \nleftrightarrow +$, $- \nleftrightarrow -$
3. $s \leftrightarrow s, a \leftrightarrow a, s \nleftrightarrow a$
4. $g \leftrightarrow u, g \nleftrightarrow g, u \nleftrightarrow u$

5. $\Delta\Lambda = 0, \pm 1$

6. $\Sigma^+ \leftrightarrow \Sigma^+, \Sigma^- \leftrightarrow \Sigma^-, \Sigma^+ \nleftrightarrow \Sigma^-$

7. $\Delta S = 0$

8. $\Delta K = 0, \pm 1$, but $\Delta K \neq 0$ for $\Sigma - \Sigma$ transition

Items 1 and 2 apply to any atomic system and item 3 applies for identical nuclei. Item 4 applies for the case of a molecule with nuclei of equal charge. Items 5 through 7 apply to both Hund's case (a) and (b). Item 8 applies only to Hund's case (b) which is the case of N_2^+ first negative system. Note that positive and negative signs in item 2 do not comply with the signs in the notation $B^2\Sigma_u^+$ or $X^2\Sigma_g^+$ since the former applies to parity properties of the total eigenfunction and the latter is for the electronic eigenfunction. K in the item 8 is the total angular momentum apart from spin that can have the integral values (K = Λ, Λ + 1,$\cdots$). Hence J, the total angular momentum including spin becomes J = K + S, K + S - 1,$\cdots$,K - S. Since S = 1/2 and Λ = 0 for N_2^+ FNS, K = 0, 1, 2,$\cdots$ and corresponding J's are 1/2, 1/2 and 3/2, 3/2 and 5/2,$\cdots$. Figure 4.1 shows the transitions between two levels. Selection rules listed above are strictly followed in the figure. Dotted lines represent transitions with equal $J's$ which will form Q branches. However, these branches follow the forms of R and P branches hence only R and P branches will be distinguishable.

Rotational energy applied to N_2^+ FNS follows general representation of

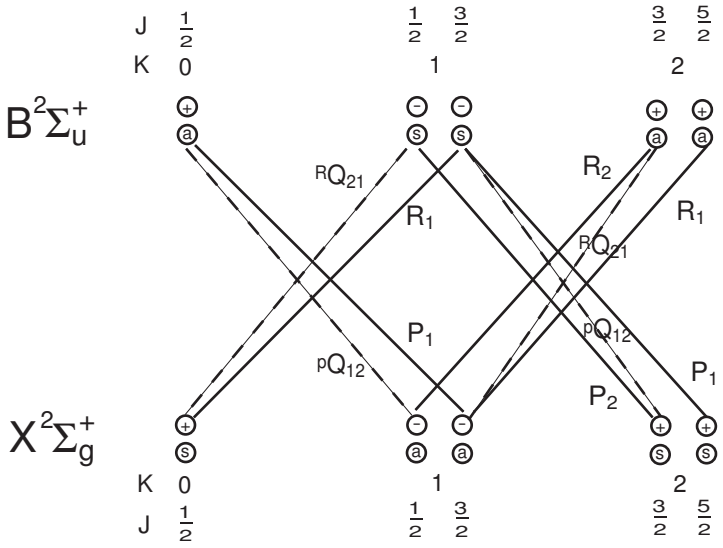

Figure 4.1: $B^2\Sigma_u^+ \rightarrow X^2\Sigma_g^+$ transition diagram with symmetry properties.

rotational term for molecule.

$$F_v = B_v J(J+1) + (A - B_v)\Lambda^2 - D_v J^2(J+1)^2. \tag{4.10}$$

The first term of Eq. 4.10 describes diatomic molecules in the rigid body rotation. The second term corrects for a symmetric top model and the last term takes care of centrifugal stretching of nuclei. Note that constants B_v and D_v are dependent upon vibrational levels but A is the same within a given electronic state so that A$\times\Lambda^2$ can be ignored when only rotational and vibrational transitions are considered. The line strength ($S_{J'J''}$) is $\frac{J'+J''+1}{2}$ and the summation of line strength for R ($\frac{J'+J''+1}{2} = \frac{J'+J'-1+1}{2} = J'$) and P ($\frac{J'+J''+1}{2} = \frac{J'+J'+1+1}{2} = J'+1$) branches becomes $2J'+1$ as discussed in Sec. 4.2.

4.4 N_2 spectra

The second positive system (SPS) of N_2 band spectra is a transition between $C^3\Pi_u$ and $B^3\Pi_g$. Transition follows Hund's coupling case (a) and selection rules that apply to this case are summarized below.

1. $\Delta J = 0, \pm 1$, but $J = 0 \nleftrightarrow J = 0$
2. $+ \leftrightarrow -$, $+ \nleftrightarrow +$, $- \nleftrightarrow -$
3. $s \leftrightarrow s, a \leftrightarrow a, s \nleftrightarrow a$
4. $g \leftrightarrow u, g \nleftrightarrow g, u \nleftrightarrow u$
5. $\Delta\Lambda = 0, \pm 1$
6. $\Sigma^+ \leftrightarrow \Sigma^+, \Sigma^- \leftrightarrow \Sigma^-, \Sigma^+ \nleftrightarrow \Sigma^-$
7. $\Delta S = 0$
8. $\Delta\Sigma = 0$
9. if $\Omega = 0$ for both states, $\Delta J \neq 0$

Item 1 through 7 are the same as N_2^+ FNS and item 8 and 9 apply only for Hund's case (a) which is the case of N_2 SPS. $\Omega = |\Lambda + \Sigma|$ and $\Sigma = S, S-1, S-2, \cdots, -S$. Since $\Lambda = 1$ and $S = 1$ for N_2 SPS, $\Sigma = -1, 0, 1$ and $\Omega = 0, 1, 2$. Since $S = 1$, $2S + 1 = 3$ states exist for both states such as $^3\Pi_0$, $^3\Pi_1$, and $^3\Pi_2$. Based on selection rule item 8 above, only $^3\Pi_0 - {}^3\Pi_0$, $^3\Pi_1 - {}^3\Pi_1$, $^3\Pi_2 - {}^3\Pi_2$

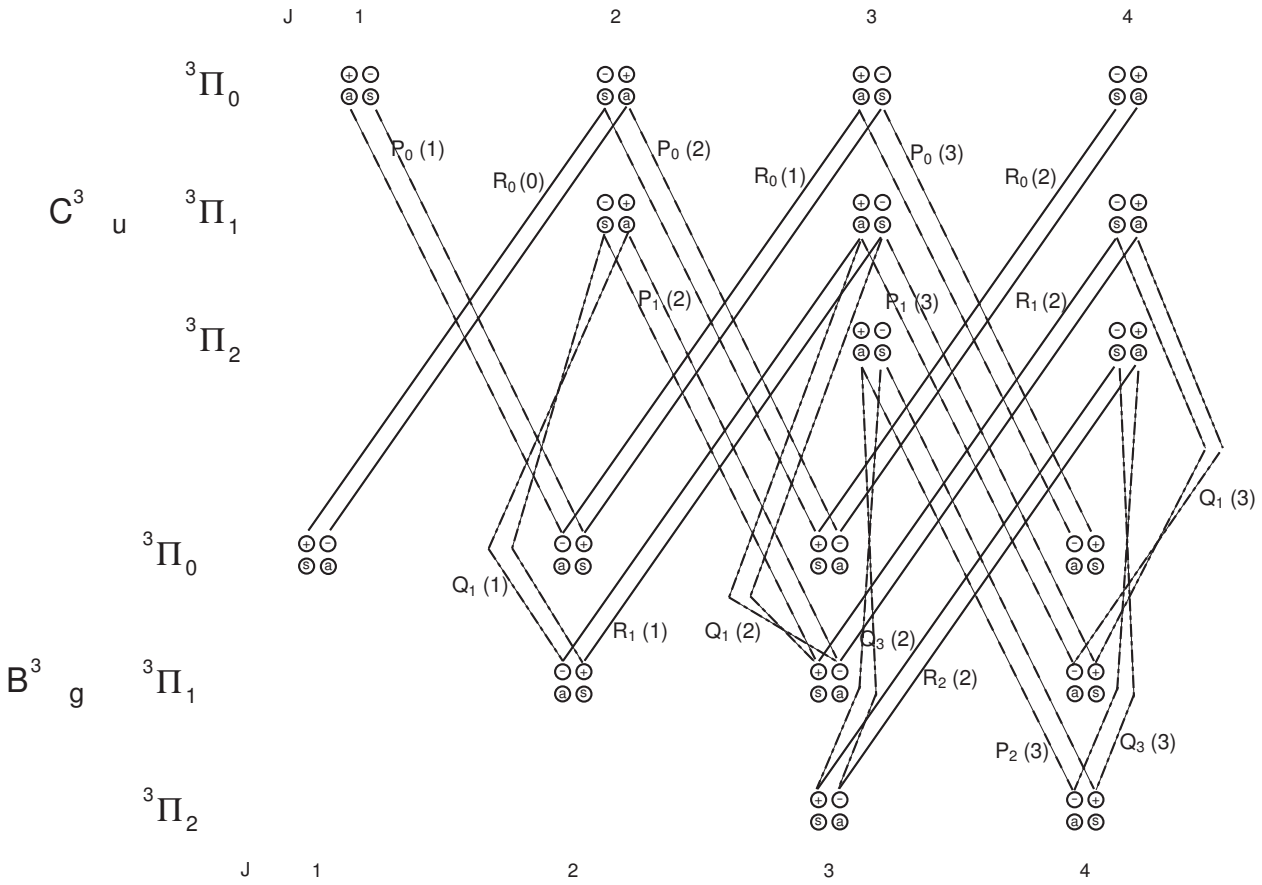

Figure 4.2: $C^3\Pi_u \rightarrow B^3\Pi_g$ transition diagram with symmetry properties.

transitions are allowed. The transition diagram is shown in Fig 4.2. Λ doubling of each rotational states is also shown. Complying with selection rule item 9 above, Q branches for $^3\Pi_0 - ^3\Pi_0$ transition are prohibited.

As most multiplet states for $\Lambda > 0$ (i.e. $\Pi, \Delta, \cdots$) exhibit a spin decoupling at high rotational energy, the rotational energy term of N_2 SPS must also incorporate a spin decoupling and these formulae are listed below (Ref. [54],

p.235).

$$F_0 = B(J(J+1) - \sqrt{Z_1} - 2\sqrt{Z_2}) - D(J - \frac{1}{2})^4 \quad (4.11a)$$

$$F_1 = B(J(J+1) + 4Z_2) - D(J + \frac{1}{2})^4 \quad (4.11b)$$

$$F_2 = B(J(J+1) + \sqrt{Z_1} - 2\sqrt{Z_2}) - D(J - \frac{3}{2})^4, \quad (4.11c)$$

where

$$Z_1 = Y_v(Y_v - 4) + \frac{4}{3} + 4J(J+1) \quad (4.12a)$$

$$Z_2 = \frac{1}{3Z_1}(Y_v(Y_v - 1) - \frac{4}{9} - 2J(J+1)) \quad (4.12b)$$

$$Y_v = \frac{A}{B_v}.$$

Hönl-London formulae for $\Delta\Lambda = 0$ are [54]

$$S_J^R = \frac{(J'' + 1 + \Lambda'')(J'' + 1 - \Lambda'')}{J'' + 1} = \frac{(J' + \Lambda')(J' - \Lambda')}{J'} \quad (4.13a)$$

$$S_J^Q = \frac{(2J'' + 1)\Lambda''^2}{J''(J'' + 1)} = \frac{(2J' + 1)\Lambda'^2}{J'(J' + 1)} \quad (4.13b)$$

$$S_J^P = \frac{(J'' + \Lambda'')(J'' - \Lambda'')}{J''} = \frac{(J' + 1 + \Lambda')(J' + 1 - \Lambda')}{J' + 1}. \quad (4.13c)$$

The summation of these three line strength formulae again gives $2J' + 1$ as for N_2^+.

4.5 Rotational and vibrational temperature measurement

4.5.1 Rotational temperature

From Eqs. 4.8 and 4.9c, the rotational line intensity is described as

$$I_{em} \sim \frac{\nu_{''}'^4 g_{J'} \Phi_{P'}}{Q_r} \exp^{-E_r'/kT_r}, \quad (4.14)$$

where $E_r^{'} = hc(F^{'} - F^{''})$ and $\nu_{''}^{'} = E_r^{'}/h$. Rotational term $F^{'}$ for N_2^+ and N_2 are calculated from Eqs. 4.10 and 4.11, respectively. Line strength $S_{J^{'}J^{''}}$ for N_2^+ and N_2 are $\frac{J^{'}+J^{''}+1}{2}$ and Eq. 4.13, respectively. Rotational partition function

$$Q_r = \sum_J g_{J^{'}} \Phi_{P^{'}} \exp^{-E_r^{'}/kT_r}$$

is constant for all rotational lines hence may not need to be calculated. Intensity alternation is noticeable for N_2^+ hence $\Phi_{P^{'}}$ is 2 for even J and 1 for odd J. But intensity alternation for the N_2 SPS is noticeable only when Λ doubling can be resolved (e.g. $^1\Pi - ^1\Pi$), thus $\Phi_{P^{'}}$ may not be considered for the N_2 SPS. Then synthetic spectra of N_2 and N_2^+ of emission intensities for all $J^{'}$ are obtained as a function of $\nu^{'}$ with a parameter of T_r.

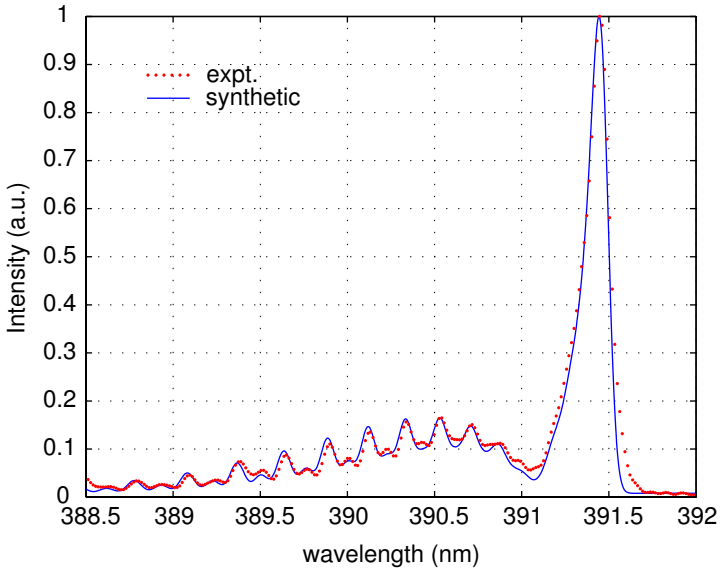

Figure 4.3: Spectral line fit of 0-0 transition of N_2^+ FNS ($B^2\Sigma_u^+ \rightarrow X^2\Sigma_g^+$) rotational band with T_r of 430 K.

Calculated synthetic spectra of N_2^+ and N_2 rotational band overlapped

with measured spectra are plotted in Figs. 4.3 and 4.4, respectively. Intensity alternation is clearly observed in Fig. 4.3 but not in Fig. 4.4 as noted above. Running average errors between synthetic and measured spectra at various T_r's are calculated as

$$\text{error} = \sum_J \frac{11\,|I_{meas,J} - I_{synth,J}|}{\sum_{i=J-5}^{i=J+5} |I_{meas,i} - I_{synth,i}|}. \tag{4.15}$$

The rotational temperature is taken as the value that minimizes the error. One can use a square error representation (e.g. $\text{error}^2 = |I_{meas,J} - I_{synth,J}|^2$). But in the case where data are highly modulated as in Figs. 4.3 and 4.4, a square error representation is likely to mismatch such a variation.

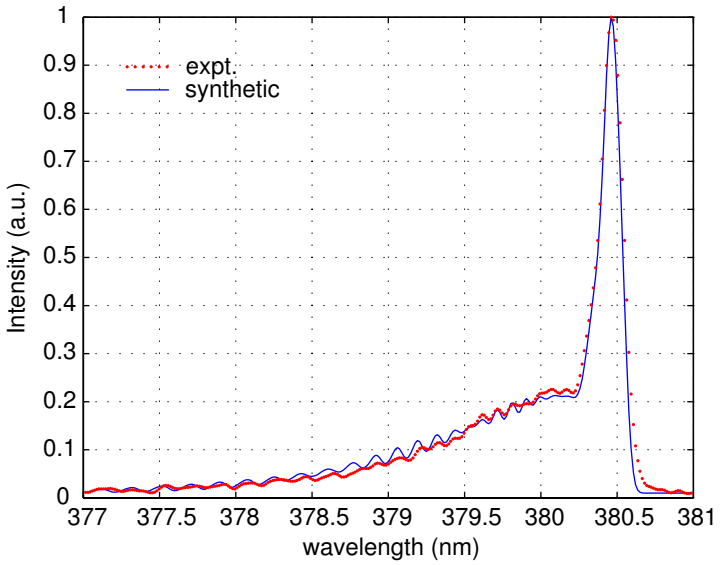

Figure 4.4: Spectral line fit of 0-2 transition of N_2 SPS ($C^3\Pi_u \rightarrow B^3\Pi_g$) rotational band with T_r of 400 K. All possible transitions from three states (Π_0, Π_1, Π_2) are considered.

4.5.2 Vibrational temperature

To obtain vibrational temperature, at least two rovibronic bands are required to be obtained. Once rotational levels for a given vibrational transition (e.g. 0-2 transition of N_2) are determined as described above, relative intensities of rotational levels for different vibrational transitions (e.g. 1-3, 2-4,$\cdots$) need to be determined. Emission line intensities of different vibrational transitions can be obtained from

$$I_{em} \sim \frac{\nu_{''}^{'4} S_{v'v''} g_{J'} \Phi_{P'}}{Q_r Q_v} \exp^{-(E_r'/kT_r + E_v'/kT_v)}. \tag{4.16}$$

Compared with Eq 4.14, the difference is $\frac{S_{v'v''}}{Q_v} \exp^{-E_v'/kT_v}$. The band strength ($S_{v'v''}$) can be found in the literature for various gases. Once the rotational temperature is estimated, the only unknown in Eq. 4.16 is vibrational temperature (T_v). By matching overall intensity (mostly the intensity of different band heads) at given T_v, vibrational temperature can be obtained. Since N_2 band shows several rovibronic bands as in Fig. 6.1 but not N_2^+, vibrational temperature is obtained from N_2 bands only.

4.6 Electronic temperature measurement

Electronic temperature (T_{elec}) determines the distribution of upper electronic state and is in close proximity with electron temperature (T_e). To obtain electronic temperature, we need several atomic lines so that the slope in Boltzmann plot can be determined. From Eqs. 4.1 and 4.9a,

$$\frac{I_{em}}{g' \nu_{''}' A_{''}'} = \frac{N_o h}{Q_e} \exp^{-E_e/kT_{elec}}, \tag{4.17}$$

Table 4.1: Spectral line database of selected Fe (I) atomic lines

wavelength (nm)	E_e $[cm^{-1}]$	degeneracy ($g^{'}$)	$A^{'}_{''}$ $[s^{-1}]$
362.15	49604.415	11	5.1e+7
364.95	49108.89	9	4.2e+7
371.99	26874.549	11	1.62e+7
382.04	33095.937	9	6.68e+7
385.99	25899.987	9	9.7e+6

where $g^{'}$ is replaced with $2S^{'}+1$ in Eq 4.9a. Taking the logarithm on both sides gives

$$ln\left(\frac{I_{em}}{g^{'}\nu^{'}_{''}A^{'}_{''}}\right) = ln(C_1) - \frac{E_e}{kT_{elec}} \cdots E_e \text{ in [J]} \quad (4.18a)$$

$$= ln(C_1) - 1.44\frac{E_e}{T_{elec}} \cdots E_e \text{ in [cm}^{-1}\text{]}. \quad (4.18b)$$

I_{em} and $\nu^{'}_{''}$ can be obtained from measured atomic spectra and $g^{'}, A^{'}_{''}, E_e$ and T_{elec} are unknowns. $g^{'}, A^{'}_{''}, E_e$ for atoms can be obtained from the NIST website [60] and are listed in Table 4.1. Now T_{elec} is the only unknown. Finally, the linear fitting of Eq. 4.18 with E_e as x coordinate is only a function of $\frac{1}{T_{elec}}$ (refer to Fig. 6.7) from which electronic temperature can be obtained.

In constricted mode 'C' discharge, several Fe (I) lines were observed due to an etching of the cathode which is made of steel. The atomic lines that are observed in this study are shown in Fig. 4.5.

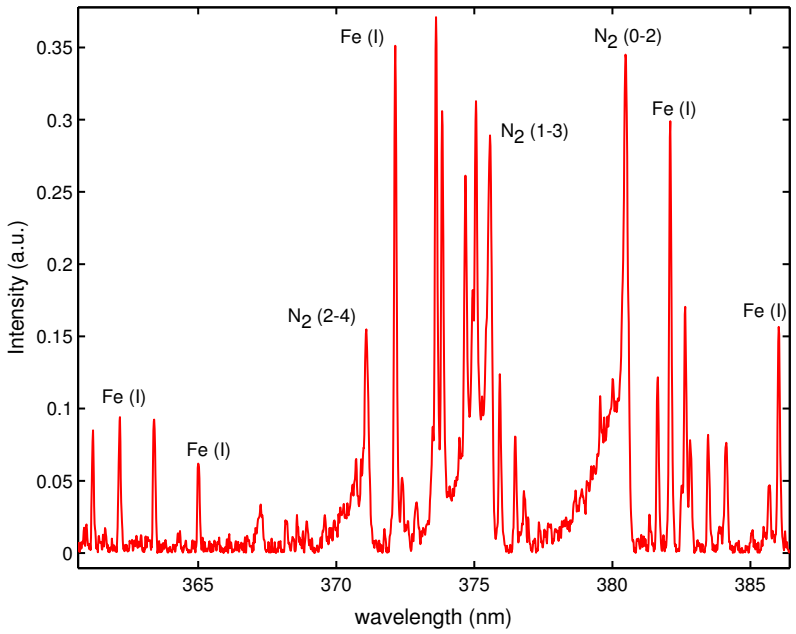

Figure 4.5: Observed Fe (I) lines. Five lines are chosen for electron temperature measurement.

Chapter 5

Supersonic flow actuation by DC surface discharge

5.1 Generation of DC surface discharge plasmas

Conventional direct-current discharges use parallel plate electrodes in closed environment with a fill gas as in discharge tubes. A DC 'glow' discharge is generated at sufficiently low pressures and is characterized by a low current ($\sim$ mA). The discharge structure of conventional parallel plate DC glow discharge has unique characteristics. Figure 5.1 shows a qualitative structure of a DC glow discharge in parallel plate configuration. Near the parallel plates

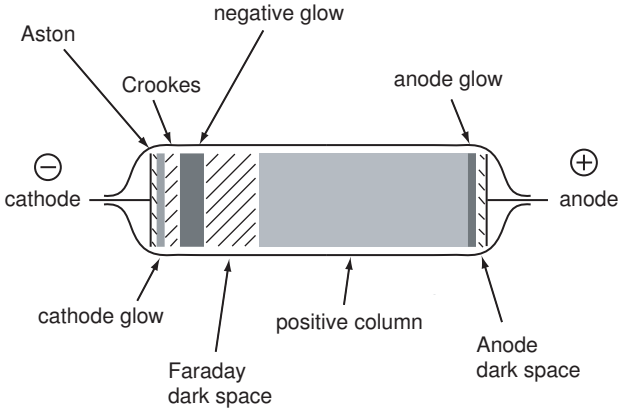

Figure 5.1: Detailed qualitative structure of a DC glow discharge in parallel plate vacuum tube. The thickness of each layer is not in actual scale.

(electrodes), a plasma *sheath* forms which is the boundary layer between the quasi-neutral plasma and electrodes. The most luminous region in the discharge is a *negative glow* where most ionization occurs. It also forms the sheath edge. The region near the cathode including negative glow is called a cathode layer. *Positive column* occupies the space between anode and sheath edge provided the distance between electrodes is long enough to form both the cathode layer and positive column. The positive column can be either visible or remain dark. When pressure becomes high, the discharge forms an arc or spark (glow-to-arc transition) [19]. An arc is characterized by high current ($\sim$ A) and high gas temperature accompanied with a significant material damage. More details about DC discharges can be found in most plasma textbooks [19, 61]. In this study, due to the geometric constraint, the actuator electrodes must be flush mounted so as not to disturb the supersonic flow as shown in Fig. 3.3.

The plasma discharge was ignited by an inter-electrode voltage drop between 500 V - 1000 V depending on the test section pressure. The power supply provided the capability to establish a set-point current through the discharge by automatically adjusting supply voltage, and set-point currents were varied from 25 mA through 300 mA. Once the discharge was initiated, the driving voltage decreased due to decreased plasma resistance (R_P). In the event of an arc, the power supply trips off to prevent drawing too much of current over the supply limit. To control the discharge regime at varying discharge conditions, the ballast resistors need to be adjusted such that smaller

resistance will bring the discharge into a high-current arc regime and a larger resistance will result in low current Townsend/glow discharge operation. Also when more than one electrode pair is used, each pair can have a different ballast resistance (R_B) so that the total impedance ($R_T = R_B + R_P$) seen by the supply is the same for each electrode pair. Since the wind tunnel is made of aluminum, parasitic secondary discharges are likely to form between anode and inner wall surface of wind tunnel or between wires. They occur typically at low pressures and in the absence of flow. In the event of secondary discharges, the main discharge between electrodes fails to turn on. In this study, thin layer (50 μm) of Kapton^{TM} tape is put along the inner wall surface of the wind tunnel. Also the center plate in the wind tunnel is made of plastic as described in Sec. 3.1. However additional care was taken to avoid possible power leak through conducting parts other than electrodes. Wind tunnel and optical table should be properly grounded for this reason.

A DC surface discharge is accompanied by significant heating of both electrodes and dielectric as well as the bulk gas. Even though the dielectric is made from high temperature ceramic material, visible evidence of heating is often observed such as erosion of the dielectric and sputtering of the electrode. Material erosion is dominant when the test section pressure becomes high ($>\sim$28 Torr). If the heating becomes significant, the dielectric can crack. Regardless of the discharge conditions, the time duration of discharge needs to be minimized to avoid significant damage of electrode and dielectric. The gas heating effect by DC surface discharge will be discussed in Ch. 6.

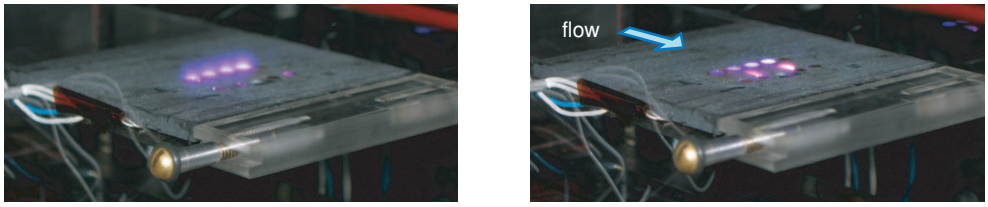

Figure 5.2: Photo images of DC surface discharge on the plasma actuator. (a) the discharge in the absence of flow. (b) the discharge in the presence of supersonic flow

Figure 5.2 shows direct photographs of the discharges inside the test section. Fig. 5.2 (a) shows four diffuse discharges on top of the cathode turned on in the absence of flow. When supersonic flow is introduced over the actuator (Fig. 5.2 (b)), the discharge structure is stretched toward the anode when the cathode is located upstream. This change in the discharge structure does not occur for every condition. The discharge structure and characteristics at different operating conditions will be discussed in the following sections.

5.2 DC surface plasma structures in the absence of a flow

As shown in Fig. 5.2 (a), a diffuse glow discharge can be obtained above cathode in the absence of a flow. It is not uncommon to observe DC discharges with luminosity that is restricted to the cathode region. For example, in a certain range of pressures and in certain geometric configurations, a DC glow discharge may have a bright luminous cathode layer corresponding to the negative glow region, whereas the positive column is either not well

formed owing to short interelectrode distance or remains less luminous or even dark [19]. The negative glow provides a visual indication of the spatial extent of the sheath-bulk plasma interface region. Note that the plasma sheath is essentially a boundary layer which connects a physical (wall) boundary and the quasi-neutral bulk plasma.

Figure 5.3 shows laser schlieren images of the discharge at different test section pressures at fixed set-point current. The sloped horizontal fringes are

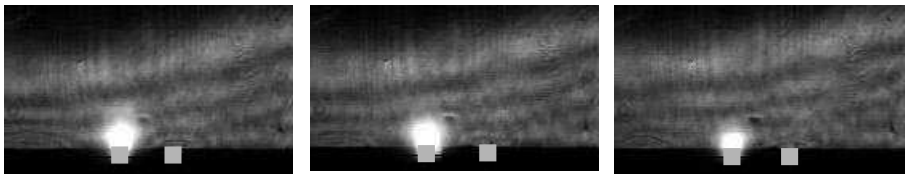

Figure 5.3: Laser schlieren images of the plasma discharge in stagnant air. Corresponding pressures are (a) 16.8, (b) 20.32, and (c) 25.4 Torr, respectively. The discharge set-point current is 100 mA for all cases. Electrode arrangement is shown as a gray block with a cathode on the left in each image.

primarily due to the diffraction from the knife edge of the schlieren setup. Electrode locations are shown as gray blocks with the cathode on the left in each image. The luminous part of the discharge is visible on top of cathode for pressures from 16.8 Torr (a) to 25.4 Torr (c) at fixed current of 100 mA. As pressure increases the volume of discharge luminous region decreases and further increase in pressure extinguishes the discharge so that a higher voltage input is required for breakdown at elevated pressures. At lower pressures ($<$ 16 Torr), it is likely to produce a secondary discharge. As test section pressure (n_g) increases, the mean-free-path ($\lambda = \frac{1}{n_g \sigma}$) decreases and hence

characteristic dimension of the glow discharge decreases. Sheath thickness is related to Debye length (λ_{Debye}) which is expressed as $\lambda_{Debye} = \sqrt{\frac{\varepsilon_o k_B T_e}{e^2 n_e}}$ and it decreases as pressure increases owing to an increase in charge density at higher pressures. Decrease in Debye length in turn is associated with a corresponding decrease in the spatial extent of the negative glow region. The observations in Fig. 5.3 are consistent with the above description of negative glow DC discharges, and thus provide some evidence that the discharge in this study is in fact a non-equilibrium glow. Figure 5.3 implies the anode location does not affect the discharge structure of parallel plate DC glow discharges upon varying test section pressure indicating the cathode layer is well confined above the cathode. It is useful to note that thermal arcs have vanishingly small sheaths and in general have a bright luminous positive column that extends from the cathode to the anode.

At a fixed pressure, the discharge current has greater effect on the discharge structure. Figure 5.4 shows luminosity images of the discharge with increasing currents in the absence of a flow at a fixed test section pressure of 16 Torr. Cathode is located on the left in each image. At 50 mA current (Fig. 5.4(a)), a luminous cathode layer similar to Fig. 5.3 is observed with the positive column being dark. As the discharge current increases, the luminous cathode layer increases in size (Fig. 5.4(b)) resulting from increasing discharge intensity (charged or excited species densities). A further increase in current (Fig. 5.4(c)) results in mode change where the diffuse discharge (with the luminous cathode layer) is replaced by a relatively constricted discharge. In this

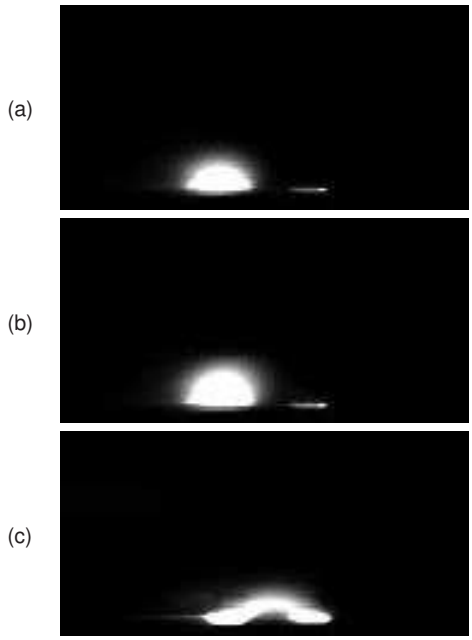

Figure 5.4: Visible luminosity images of the discharge in the absence of flow at a fixed pressure of 16 Torr. The input currents are (a) 50 mA, (b) 150 mA, and (c) 200 mA, respectively.

constricted discharge, the current density suddenly increases with increasing charge densities and a smaller Debye length. The anode glow is visible in Fig. 5.4 (a) and (b). The constricted discharge mode is characterized by a luminous positive column that spans the entire length between the cathode and the anode. The structural change into a constricted discharge is originated from the plasma instability in the diffuse mode. A mode change of this nature where diffuse glow discharge self-constricts above a certain threshold current is well documented in the literature (see Ref. [62], pg. 474). It is also well established that the constricted mode is not necessarily a thermal arc since the discharge continues to be non-equilibrium in the constricted mode, with the

charge densities remaining well below typical densities for an arc. The constricted mode is therefore still a glow mode, albeit with higher charge densities than the diffuse glow mode. This mode change can therefore be characterized as a diffuse-to-constricted glow mode transition. At much higher current ($>\sim$ 300 mA) secondary parasitic discharges occurs between the electrodes and the grounded test section walls, thereby establishing a practical upper limit to the discharge currents. Also a constricted discharge is accompanied by material damage of electrode and dielectric material.

5.3 DC surface plasma structures in the presence of a flow

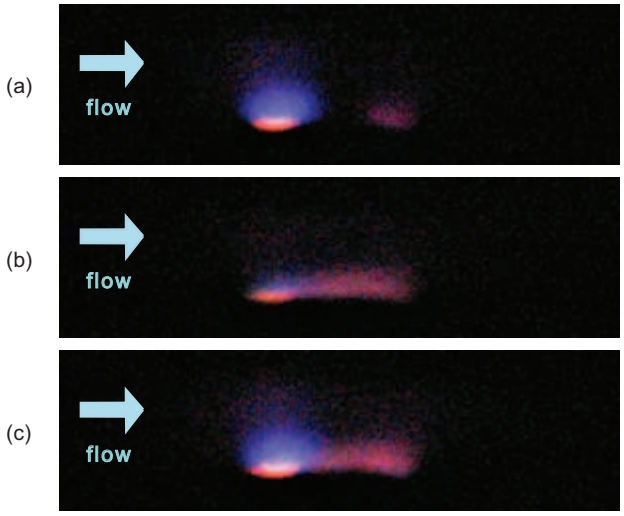

Figure 5.5: Images of different discharge structures in the presence of a supersonic flow. Cathode is located left in each image. Discharge conditions are; (a) mode D - diffuse for 100 mA and 16 Torr, (b) mode C - constricted for 150 mA and 25 Torr and (c) mode M - mixed for 150 mA and 15 Torr.

Figure 5.5 presents visible true color images of the discharge at different conditions in the presence of the supersonic flow. The flow is from the left to the right in each image (the cathode being on the left). Figure 5.5(a) is for a 100 mA discharge with a test section static pressure of 16 Torr, Fig. 5.5(b) is for 150 mA and 25 Torr, and Fig. 5.5(c) is for 150 mA and 15 Torr. At lower current and lower pressure (Fig. 5.5(a)), the diffuse discharge with the luminous cathode layer (negative glow) is observed. The cathode layer has a distinct bluish color as seen in the image. This structure is similar to Fig. 5.4 (a) and (b) indicating that under certain conditions the discharge structure is not affected by the presence of a supersonic flow. Similar diffuse discharge structure at Mach 5 flow can be found in the literature [63]. Note that Mach 5 flow has lower static pressure than Mach 3 flow which in turn results in more diffuse discharges. Increasing the current and test section pressure to 150 mA and 25 Torr, respectively, results in a mode change where only the positive column in a relatively constricted discharge is visible (Fig. 5.5(b)). The positive column has a distinctive pink color indicating that different species are excited in the positive column compared to the luminous cathode layer in the case of the diffuse glow. This structure is again similar to Fig. 5.4 (c) but more flattened toward surface. For conditions with the same current (150 mA) as in Fig. 5.5(b), but at lower pressure (15 Torr), the discharge exhibits a bistable state where both the diffuse mode (with a luminous cathode layer) and the constricted mode (with a luminous positive column) are observed in the same image frame. This bistable state discharge is observed to rapidly switch be-

tween these two modes, giving a visual (time-averaged) appearance that both a constricted positive column and a diffuse cathode layer occur simultaneously. Schlieren imaging (both flash lamp and laser) applied to this bistable discharge shows individual images that resemble both Fig. 5.5(a) and Fig. 5.5(b) and occasionally show images of the 'mixed mode' with both constricted positive column and the diffuse cathode layer visible in the same image. In all cases studied so far with supersonic flow, the overall discharge structure can be characterized by either one of the two modes (diffuse or constricted), with a third bistable state comprising a combination of the diffuse and constricted modes. It is convenient to classify the two modes as 'mode D' (for diffuse glow discharge with the luminous cathode layer, as in Fig. 5.5(a)) and 'mode C' (for constricted glow discharge with a luminous positive column, as in Fig. 5.5(b)) and additional bistable 'mode M' (for bistable/mixed mode where both the cathode layer and the positive column are luminous in a time-averaged sense, Fig. 5.5(c)). Note that similar to Fig. 5.4 (c), constricted mode C discharge is also a glow (abnormal glow) discharge and not an arc since the current density is much lower than that of an arc. In the presence of external magnetic field, these discharge structures can be altered by a Lorentz force [63].

Figure 5.6 provides a schematic illustration of the luminous regions corresponding to each mode presented above. At pressures greater than about 25 Torr, the discharge remains largely in the constricted mode C, whereas the discharge remains mostly diffuse (mode D) at lower pressures. Note that the size of the luminous region of the discharge does not change substantially

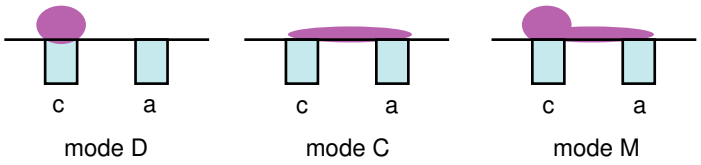

Figure 5.6: Different discharge modes in a supersonic flow. Label 'a' and 'c' denote the anode and cathode, respectively. Flow direction is from left to right. The mode D is a diffuse discharge with a luminous cathode layer, mode C is a constricted discharge with a luminous positive column, and mode M is a bistable mixed mode comprising both mode D and mode C in a time-averaged sense.

either in the presence or absence of flow, as long as the discharge remained diffuse mode D (compare Figs. 5.4 (a) and 5.5 (a)). It can be inferred from the above discussion that there is a definite pressure and current range over which the discharge remains diffuse and this current range becomes wider in the presence of flow due to aerodynamic stabilization (p. 243 in Ref. [19]). For example, the operating discharge current is practically less than 150 mA in the absence of a flow but it becomes as high as 300 mA - 400 mA in the presence of supersonic flow. If pressure becomes high with the constricted mode discharge, luminous region can be convected further downstream of electrode location resulting in a plasma tail-like feature. This mode of operation is also accompanied by cathode sputtering resulting in bright point-spots convecting downstream. Similar result is observed in modelling study by Deconinck *et al.* [64] where charged species convect downstream driven by a supersonic flow. In high-pressure and high-current arc discharges, this luminous region convecting downstream of electrode location is often observed [65].

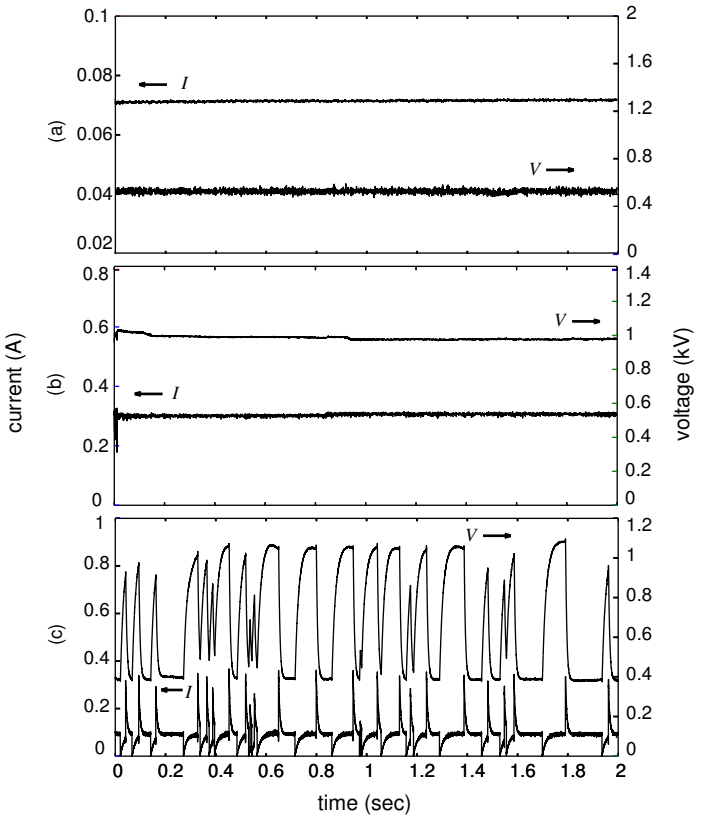

Figure 5.7: Time records of discharge current and voltage drop across the DC discharges in the presence of a supersonic flow. (a) 75 mA, (b) 300 mA, and (c) 150 mA, power supply set-point currents. The static pressure is maintained approximately at 16 Torr for all the cases.

Different discharge modes exhibit different current-voltage (I-V) characteristics. Figure 5.7 shows representative time-traces of the discharge current (I) and discharge voltage drop (V) transients during a short period (2 sec) of a typical run. Transient data is low-pass filtered to reduce electrical noise. These transients are all for cases with the discharge in the presence of the supersonic flow and with a constant test section pressure of 16 Torr. As shown

in Fig. 5.7(a), at a relatively low power supply set-point current (75 mA), voltage drop across the discharge is about 0.5 kV and both discharge current and voltage drop remain relatively steady in time. The discharge total resistivity under these conditions is about 6.6 kΩ and the total power dissipated in the discharge is about 37 W. Time-resolved schlieren images taken under these conditions confirm that the discharge is stable in a diffuse mode D. Figure 5.7(b) shows the case of a high set-point current of about 300 mA, and it is seen by time-resolved schlieren imaging that a steady discharge corresponding to mode C is obtained. Here the discharge potential drop is about 1 kV and the discharge current is at the set-point current of 300 mA. The discharge resistivity in this constricted mode is about 3.3 kΩ, which is half the resistance of the diffuse mode. The total discharge power is however 300 W, which is about an order of magnitude greater than for the diffuse mode. For an intermediate power supply set-point current of 150 mA (Fig. 5.7(c)), the current-voltage transient reflects the bistable mode M discharge. The discharge is seen to abruptly transition from one mode to another with relatively long time periods of order hundreds of milliseconds during which the discharge remains stable in a particular mode. It is clearly seen from the transients that during periods when the discharge remains at the set-point value of about 150 mA, the discharge voltage can be either close to 1 kV or around 0.4 kV, reflecting the high resistivity (mode D) and low resistivity (mode C) states, respectively. Immediately following a mode transition (as indicated by sharp spikes in the current transient, which occurs almost instantaneously on the transient time

scale shown in the figure) the power supply responds by either increasing or decreasing the power supply voltage to maintain the current at the set-point value. The discharge voltage transient is determined by the response time of the power supply, which is of order 10 μs. These transient profiles are also consistent with the schlieren images of the mixed mode M discussed earlier. For these intermediate current conditions individual schlieren images occur in one of mode D or mode C, and occasionally images having both a luminous cathode layer and positive column are observed as a consequence of a mode transition during the exposure time of the image frame. Regardless, it must be emphasized that the bistable mixed mode M at intermediate currents or pressures is a consequence of the nature of the power supply being used in our study, which tries to control the discharge current to a set-point value.

5.4 Plasma-induced flow actuation

As we have seen in the previous section, a DC glow surface discharge can exhibit different modes (mode D, C and M) in the presence of a supersonic flow depending on the discharge operating conditions and flow conditions. These discharge modes are also observed to have different interactions with the oncoming supersonic flow and consequently "actuate" the flow differently. Figure 5.8 shows three flash lamp schlieren images of the flow field structure of the Mach 2.85 supersonic flow in the presence of the DC surface discharge. The frame-rate of the imaging is 60 Hz. The discharge current and pressure are 100 mA and 16 Torr for Fig. 5.8(a), 150 mA and 20 Torr for Fig. 5.8(b), and 150

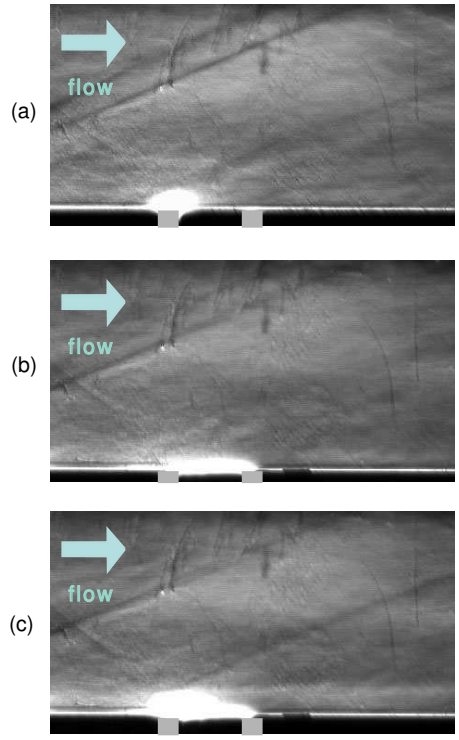

Figure 5.8: Flash lamp schlieren images of flow interaction with DC surface discharge. (a) 100 mA and 16 Torr, (b) 150 mA and 20 Torr, and (c) 150 mA and 16 Torr. Flow direction is from left to right. The weak shock waves are observed in (a) and (c) but not in (b).

mA and 16 Torr for Fig. 5.8(c), respectively. The corresponding discharges are in mode D for Fig. 5.8(a), mode C in Fig. 5.8(b) and mode M in Fig. 5.8(c). For conditions corresponding to the diffuse mode D discharge (Fig. 5.8(a)), a perceptible effect of the discharge is observed on the flow through a weak oblique shock originating from the discharge region. The weak shock is completely absent in the case of a constricted mode C occurring at higher pressures and currents (Fig. 5.8(b)), indicating that the flow is unaffected by the dis-

charge for this condition. This however does not preclude the possibility that the constricted mode C discharge does affect the pressure profiles in the near discharge region, although clearly the effect of this near discharge interaction is not evident in a far field shock emerging from the discharge region. The schlieren image for the mixed mode M (Fig. 5.8(c)) also shows the presence of plasma-induced oblique shock. For operating conditions corresponding to Fig. 5.8(c), the shock is observed to be present for images with the discharge in mode D and absent for images with discharge in mode C. This indicates that for all conditions it is necessary for the discharge to remain in the relatively low power ($\sim$10 W) diffuse mode D rather than the higher power ($\sim$100 W) constricted mode C in order to produce a visible effect of plasma flow actuation. Similar observation is found from surface pressure measurements of Kimmel *et al.* [6], who reported that an increase of surface pressure just downstream of the cathode was much higher in the case of a low current diffuse discharge compared to a more constricted discharge at higher currents. Our observations are highly repeatable and is confirmed through multiple experimental runs. Therefore, based on our schlieren imaging evidence of a shock emerging from the discharge region and consistent observations on the surface pressures measured by Kimmel *et al.* [6], the visible weak shock can be used as a measure of the effectiveness of plasma-flow interaction. Also note that generation of discharge-induced flow actuation (discernible as shocks originating from the discharge location) has, however, been reported at much higher power (a few kW) in filamentary arcs [66] where gas temperatures are high

and dilatation effects are expected to be the only dominant mechanism of flow actuation in the absence of magnetic fields [6]. This implies that in constricted mode C discharge the input current must be much higher ($\sim$ 1's A) to produce a discernable weak interaction shock. On the other hand, the diffuse mode D discharge is much more efficient producing an interaction shock.

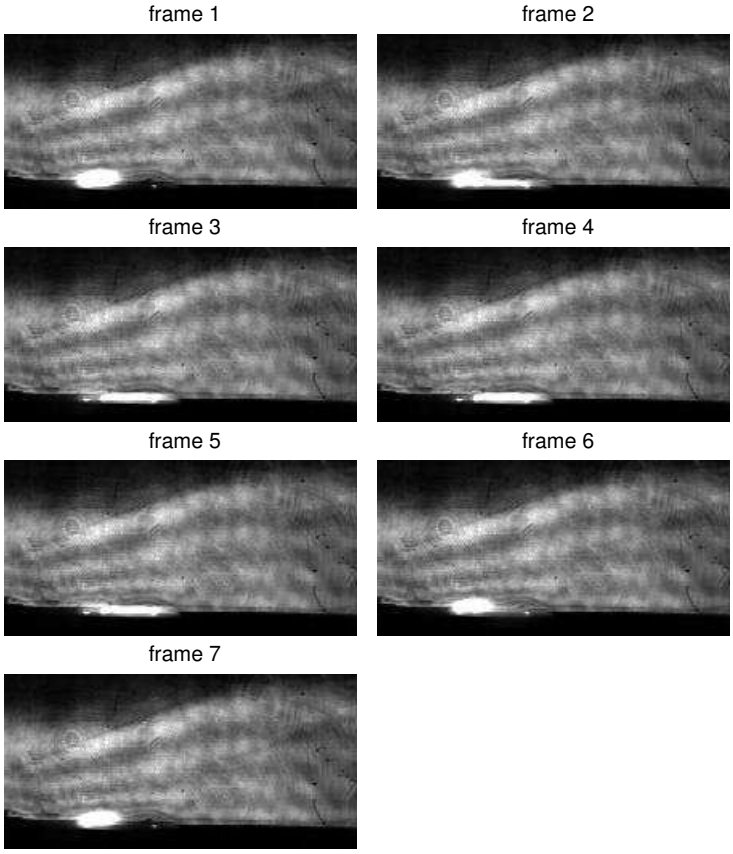

Figure 5.9: Time-resolved frame-by-frame laser schlieren images of plasma induced shock at 4.5 kHz framing rate. 140 mA of input current at static pressure of 16 Torr.

As mentioned in Ch. 1, flow actuation by plasma is characterized by

high bandwidth actuation. To confirm this, instantaneous snapshots of the discharge structures are recorded frame-by-frame using high speed laser schlieren (Fig. 5.9). For conditions corresponding to the bistable discharge mode M in Fig. 5.8(c), the frame-by-frame schlieren images reveal that a discharge-induced shock appears within one frame after the discharge switches from the constricted mode C to the diffuse mode D. Similarly, the shock disappears within one frame after the discharge switches from diffuse mode D to constricted mode C. In frame #1, diffuse mode D discharge forms and corresponding weak shock is produced. In frame #2, a switch of discharge mode from mode D to mode M occurs and weak shock is still observed. But in frame #3 where the discharge mode is switched into constricted mode C discharge, weak shock disappears. This event occurs between two frames in which the time scale is 222 μsec. Constricted mode C discharge continues until frame #5 and weak shock is absent for these frames. In frame #6, discharge structure starts to recover to diffuse mode D discharge and weak shock is emerging from cathode region. In frame #7 diffuse mode D discharge is established and weak shock is present. This observation indicates that the discharge mode switch occurs within the time period of 222 μs for each frame of the camera as was confirmed by the electrical characteristics of the mode M discharge in Fig. 5.7(c). More importantly, these images show that flow actuation occurs on time scales shorter than the framing rate of the laser schlieren imaging, indicating that less than 100 μs flow actuation is indeed possible with plasma actuators. Clearly, either electrostatic forcing or rapid volumetric gas heating

is responsible for the fast flow actuation phenomena. Also, the rapid time-scales of actuation conclusively eliminate surface heating as the cause of flow actuation. Menart *et al.* [44] showed that the effect of surface heating is an order of magnitude slower than volumetric heating by the plasmas. More importantly, above results indicate that to obtain significant flow actuation in a localized DC surface glow discharge the plasma must be operated in a relatively low power diffuse mode D, which implies a limited set of pressure and discharge power conditions under which glow discharge based supersonic flow actuation is possible. Operating at higher powers resulted in a constricted discharge mode that was found to be relatively ineffective in flow actuation. For conditions under which the diffuse mode D glow discharge is not stable (higher pressure condition), flow actuation is more effectively achieved at much higher powers ($\sim$ kW's) where filamentary arcs are generated [8].

5.5 Scaling up the actuation

It is expected that the higher power discharge can produce a bigger disturbance. In normal glow discharge regime, plasma discharge power increases linearly with increasing current since the discharge voltage remains roughly constant as current increases. But the diffuse mode D discharge in this study is in the abnormal glow regime. Therefore, the discharge power increases more rapidly than linear with increasing current. Figure 5.10 presents schlieren images at different discharge currents. Static pressure is set at 16 Torr for both cases. Figure 5.10 (a) and (b) exhibit diffuse mode D discharge and conse-

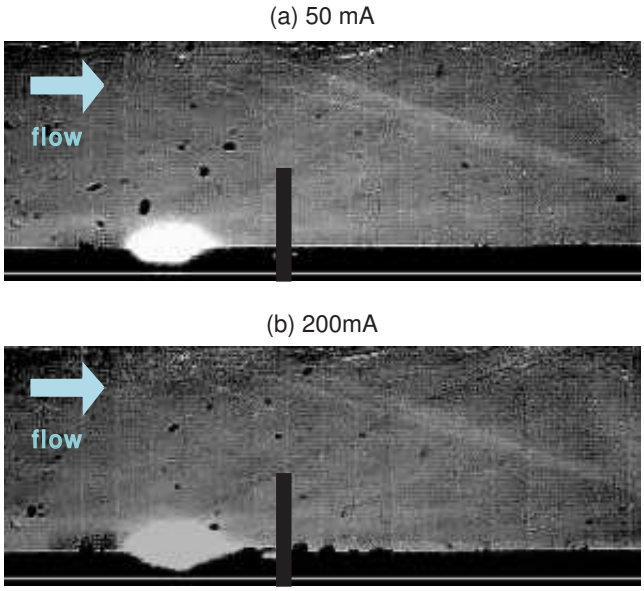

Figure 5.10: Schlieren images of induced oblique shock with increasing current at fixed pressure of 16 Torr. Vertical bars are placed in the same location with respect to cathode for each image and compare the locations of oblique shock at different currents.

quently show weak oblique shock. However, at higher current (Fig. 5.10 (b)) the shock is seen to be stronger than the lower current case. Vertical bars shown in each image are identical in size and placed at the same location with respect to cathode. They provide a comparison of relative shock location in each image. It can be seen in Fig. 5.10 (b) that at higher current the oblique shock is slightly more elevated and forms closer to the discharge region. This result partly demonstrates that the effect of flow actuation can be scaled up by increasing discharge current. Importantly, it is shown that arbitrarily large current makes the discharge more constricted and the actuation is no longer achieved. This actuation limit can be overcome by increasing the number of

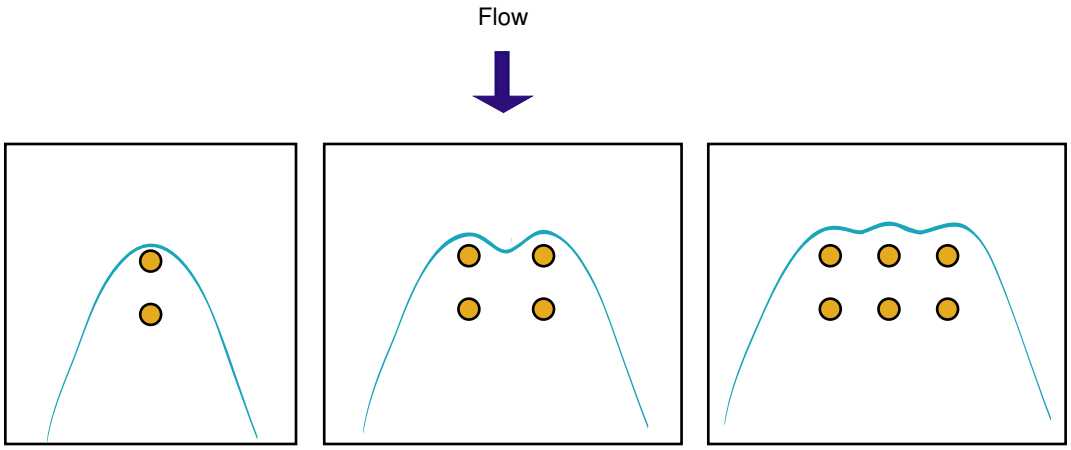

Figure 5.11: Schematic showing the effect of increasing the number of electrode pair. Single pair produces a 3D bump-like disturbance while two and more pairs produce a 2D wedge-like disturbance.

electrode pairs within a certain current regime where the diffuse mode D discharge can be obtained at relatively low power. Figure 5.11 illustrates the effect of large area flow actuation by increasing the number of electrode pairs. With a single electrode pair, the discharge produces a 3D bump-like disturbance to the flow with significant 3D relieving effect. As the number of pairs increases, the disturbance becomes more 2D wedge-like by overlapping 3 dimensional interactions produced by individual discharge pair. This effect is clearly seen in schlieren images presented in Fig. 5.12. Vertical bars again provide relative location of the shock in each schlieren image. The discharge is in diffuse mode D discharge for each electrode pair. As the number of electrode pairs increases, induced oblique shocks become more distinguishable and are more elevated indicating stronger shock and hence a stronger plasma-flow interaction near the cathode region. This implies an important advantage of

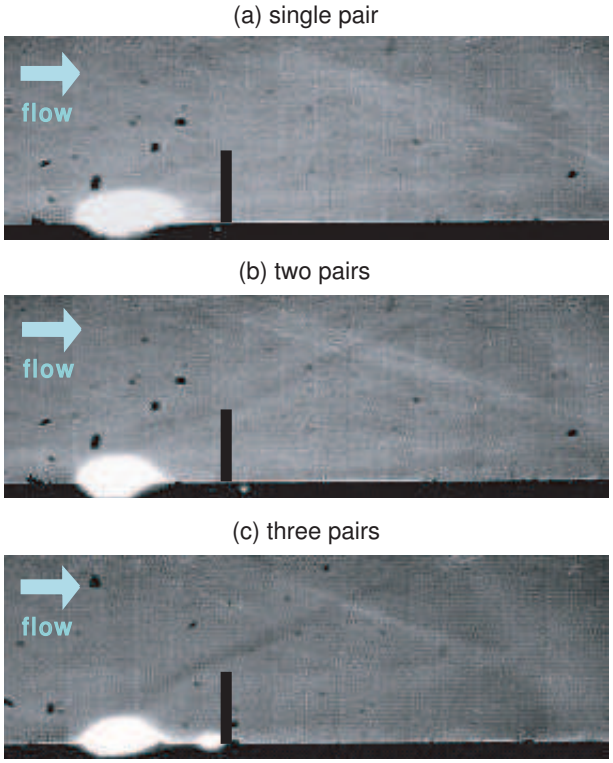

Figure 5.12: Schlieren images of induced oblique shock with increasing number of electrode pairs at fixed pressure of 16 Torr. Discharge current is 100 mA for each pair. Vertical bars are placed in the same location with respect to cathode for each image and compare the locations of oblique shock at different currents.

glow discharge plasma actuator since even in multiple number of electrode pairs total discharge power (for example, about 200 W for Fig. 5.12 (c)) is still not significant. For filamentary arc discharges large area actuation is not practical because of prohibitive total power requirement. Therefore, when large area of actuation is desired, glow discharge actuator is more promising.

The results presented so far were for the cathode in the upstream loca-

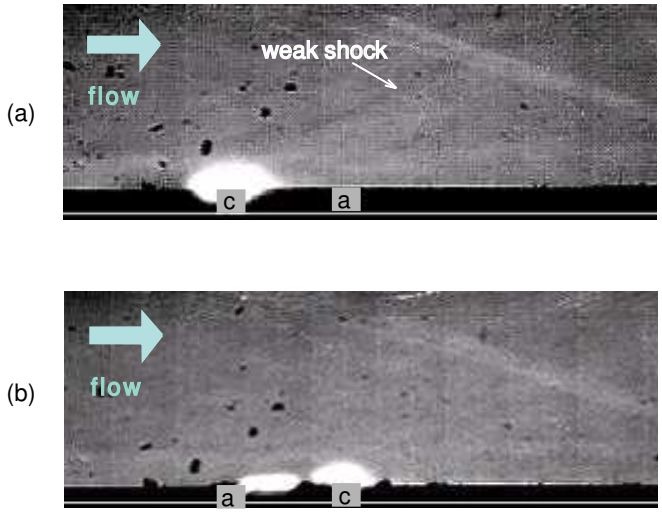

Figure 5.13: The effect of cathode location on the flow actuation. (a) cathode location upstream of supersonic flow and (b) cathode location downstream of supersonic flow. Discharge current is 50 mA and static pressure is about 16 Torr for both cases.

tion. When the electrode polarity switches from cathode upstream to cathode downstream, the discharge structure and operating regime change. Figure 5.13 shows the schlieren images showing the effect of electrode polarity. Fig. 5.13 (a) is the case with the cathode located upstream and Fig. 5.13 (b) is with the cathode downstream. The discharge current is 50 mA each case and two pairs of electrode are turned on at pressure of about 16 Torr. Fig. 5.13 (a) shows the weak oblique shock produced by the discharge with the cathode located upstream (same as presented so far), while Fig. 5.13 (b) shows no discernable shock produced by the discharge with the cathode located downstream. This is partly because the discharge structure is a diffuse mode D for Fig. 5.13 (a) and a mixed mode M for Fig. 5.13 (b). However, from the observation in

Fig. 5.8 (b), even mixed mode M discharge exhibits a shock. This implies that the cathode downstream case produces weaker actuation at a given discharge current. With a cathode located downstream, the discharge current should be as high as about 300 mA to produce a discernable shock, while with a cathode located upstream an oblique shock is discernable at the discharge current as low as 50 mA. Also the discharge structure is dominantly a mixed mode M discharge for most of cathode downstream cases. This result clearly indicates that the cathode location plays a big role in a supersonic flow control. If the inter-electrode distance is too large, one can expect that the local flow properties such as local Reynolds number may differ when cathode location is switched which in turn produces different flow actuation. However, in this study the inter-electrode distance is only 0.3 inches and hence any changes in flow properties are not expected with the change in the cathode location. A similar result was reported in Ref. [67] where the surface pressure measurement showed negligible effect with the cathode located in the downstream of the flow. Assuming that gas heating for both cathode upstream and downstream are similar because of the same input power, electrostatic forcing is expected to play a role in a supersonic flow actuation from the result of cathode downstream actuation. The details of actuation mechanism for cathode downstream and cathode upstream locations will be discussed in the following chapter.

Chapter 6

Study of flow actuation mechanisms by the discharge

In the previous chapter, DC surface discharges and their interaction with oncoming supersonic flow were presented. It was shown that a diffuse mode D glow discharge is essential to achieve flow actuation in supersonic flow. In this chapter, the investigation of the actuation mechanisms by a DC surface glow discharge will be presented. As mentioned in the introduction, in the absence of an external magnetic field, the actuation of supersonic flow by the DC glow discharge is achieved either by electrostatic forcing or dilatational effects owing to gas heating. The following sections will discuss these actuation mechanisms in greater detail and seek to understand the actuation phenomena by DC surface glow discharges.

6.1 Gas heating effect by DC surface discharge

6.1.1 Spectra of air plasma and nitrogen rovibronic bands

In DC surface discharge plasma actuator, gas heating and the corresponding dilatation effect are important actuation sources to create a disturbance in a flow. To provide further insights into the potential role of dilatational effects it is important to know the translational (gas) temperature of

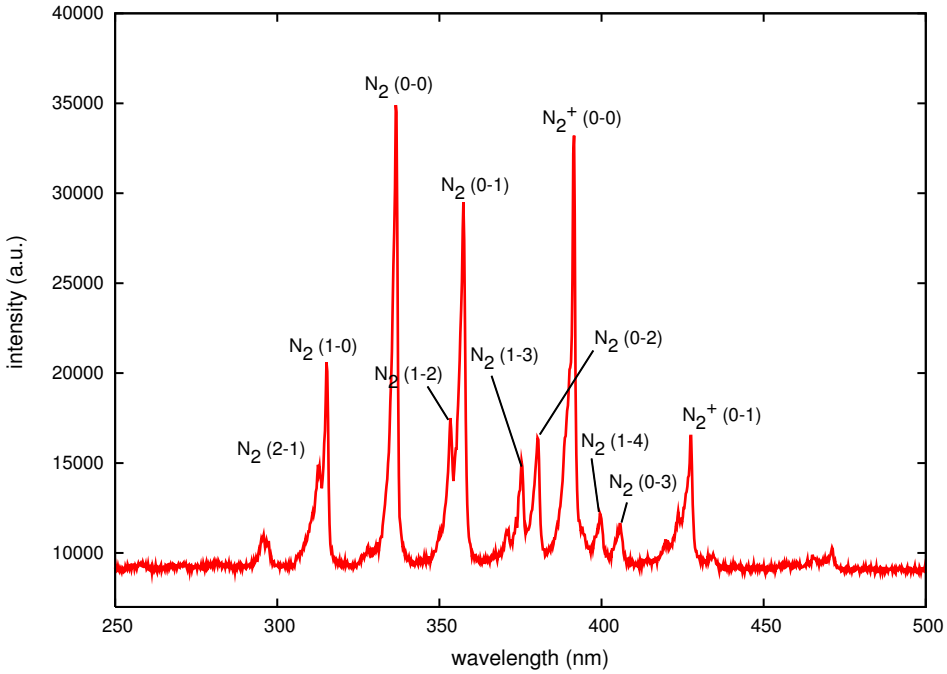

Figure 6.1: Emission spectra of air plasma in a stagnant condition.

heavy species in the plasma. Since relatively high-pressure plasmas, such as the one investigated in this study, enable a fast rotational-translational energy transfer, the rotational temperature of the bulk gas can be assumed equal to gas temperature. In plasmas, direct measurements, e.g. via thermocouples, is not possible because of the ionized gas environment. Hence, non-intrusive optical emission spectroscopy of the discharge is commonly used to estimate the rotational temperature of molecular species in the discharge. In this study, nitrogen band systems are studied because they can be easily identified in nitrogen carrying plasmas [49] and extensive reference data are available in the literature [21, 50–53]. More detail on nitrogen molecular spectroscopy is

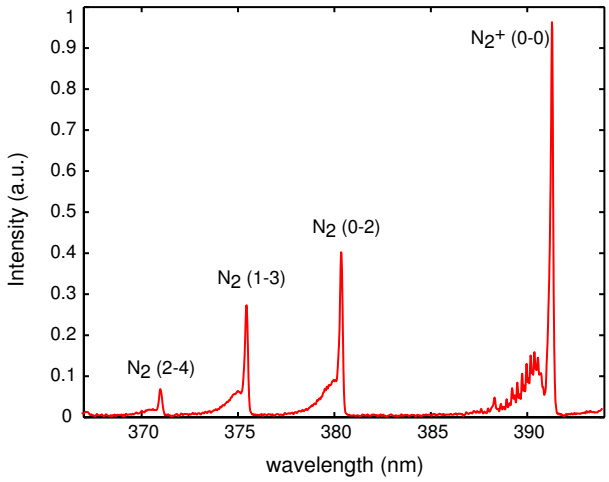

Figure 6.2: Emission spectra of air plasma in a Mach 3 supersonic flow. The current input is 50 mA with diffuse mode D discharge.

presented in Ch. 4.

Figure 6.1 shows the emission spectra of air plasma in stagnant conditions. The numbers in parentheses represent vibrational quantum numbers (v) of upper and lower state. For example, N_2 (1-0) means a transition from $v' = 1$ to $v'' = 0$. As shown in Fig 6.1 many nitrogen molecule and nitrogen ion lines are observed in the range between near UV and the blue. No other atomic or molecular spectra such as NO, O_2, or OH are detected between 200 nm and 800 nm. Among those nitrogen lines, a range between 365 to 395 nm is studied in detail because several N_2 vibrational transitions (0-2, 1-3, 2-4) can provide a vibrational temperature, and N_2 (0-2) and N_2^+ (0-0) rotational bands can provide a rotational temperature as well.

Figure 6.2 shows the emission spectrum of nitrogen rovibronic band systems in the wavelength range from 365 to 395 nm, in the Mach 2.85 su-

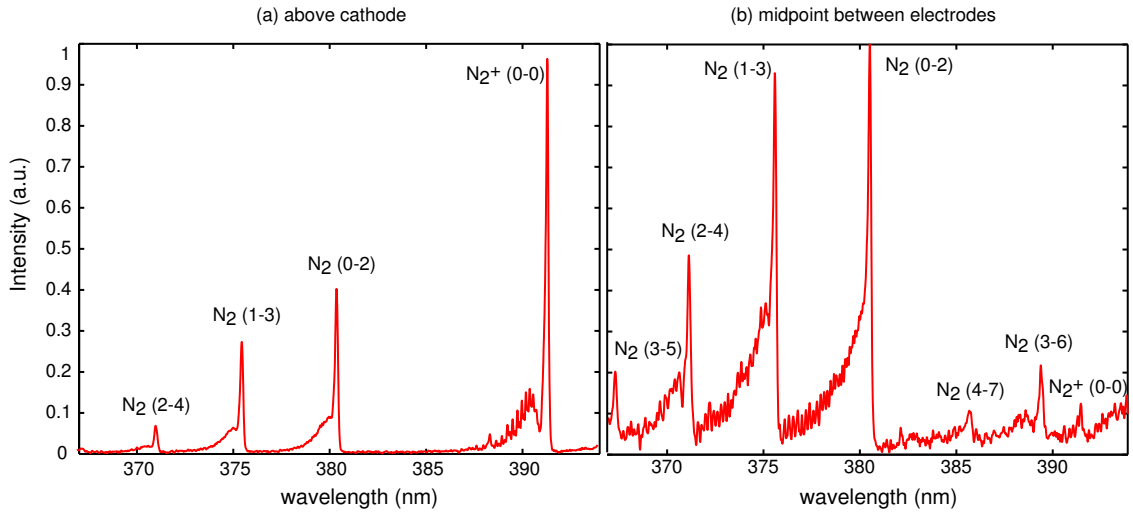

Figure 6.3: Emission spectrum of constricted mode C discharge in a Mach 2.85 supersonic flow in the wavelength range from 365 nm to 395 nm. (a) above cathode and (b) in the middle between cathode and anode. The discharge current is 75 mA.

personic flow. The spectrum is measured just above the cathode surface. The discharge set-point current is 50mA and the discharge structure is in the diffuse mode D. The N_2^+ first negative system ($B^2\Sigma_u^+ \rightarrow X^2\Sigma_g^+$) at 391.44nm (0-0) and N_2 second positive system ($C^3\Pi_u \rightarrow B^3\Pi_g$) at 380.49 nm (0-2), 375.54 nm (1-3) and 371.05 nm (2-4) are observed. Rotational lines are much more distinguishable for the N_2^+ band compared to the N_2 bands. Since the diffuse mode D discharge produces emission only near the cathode, spectra are measured only in the negative glow region. The corresponding emission spectra of the constricted mode C discharge at a current of 75 mA are shown in Fig. 6.3. Figure 6.3(a) is the spectrum measured above the cathode and Fig. 6.3(b) is measured just above the surface approximately midpoint between the anode

and the cathode. Note that the relative intensities of two cases are normalized by the peak intensity lines (e.g. N_2^+ (0-0) in Fig. 6.3(a) and N_2 (0-2) in Fig. 6.3(b)). Just above the cathode (Fig. 6.3(a)), emission from the N_2^+ (0-0) band is much stronger than that from the N_2 bands and the spectrum is similar to that taken at the same location for the diffuse mode D discharge (Fig. 6.2). The intensity of the N_2^+ band decreases significantly when measured in the positive column for the constricted mode C discharge (Fig. 6.3(b)). The differences in the relative intensities of the N_2^+ (0-0) band and the N_2 bands at different locations are reflective of significant compositional differences in the different regions of the discharge; here the positive column and the cathode layer. This is also responsible for the different luminous colors of the positive column and cathode layer as seen in the discharge structure images in Fig. 5.5. Note that the N_2 bands can be observed in most of the cases due to its large oscillator strength and large population in air [68].

6.1.2 Temperature estimation

Rotational temperatures are estimated by fitting calculated synthetic spectra to the measured N_2 and N_2^+ rovibronic emission spectra. The N_2^+ rotational band is simulated assuming Hund's coupling case (b) and accounting for the intensity alternation owing to nuclear spin [54]. The N_2 rotational band is simulated using a representation intermediate between Hund's coupling cases (a) and (b) since the N_2 band conforms to Hund's case (a) at low rotational quantum numbers and case (b) at high rotational quantum numbers [54]. The

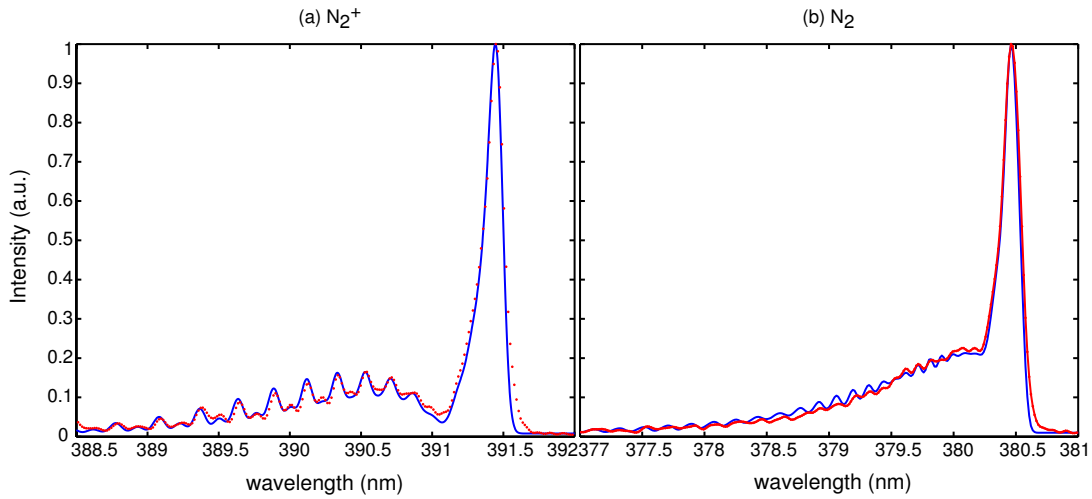

Figure 6.4: Spectral line fits of (a) N_2^+ and (b) N_2 rotational bands for a 50 mA diffuse mode D discharge in a Mach 2.85 supersonic flow. Dotted line is the measured spectrum and solid curve is the synthetic spectrum. N_2^+ fit estimates 430 K and N_2 estimates gives 400 K.

resulting spectral lines are convolved with a Gaussian instrument broadening profile whose full-width at half maximum (FWHM) is measured as 0.083 nm using a He-Ne laser. Doppler broadening ($\lambda_{Doppler} = \lambda_o 2\sqrt{2ln2\frac{kT}{mC^2}}$) is estimated to be three orders of magnitude smaller than instrument broadening. Stark broadening is neglected under the relatively low electron density ($<10^{13}$ cm^{-3}) conditions expected for the discharge in this study. Figure 6.4 shows spectral line fits of N_2^+ and N_2 rotational bands of the 50 mA diffuse mode D discharge in the presence of supersonic flow at test section static pressure of 16 Torr. Almost all the peaks and valleys of the rotational lines match well in the N_2^+ fit. However in the N_2 fit, only the overall shape and line positions agree. This is because the gas temperature is low and hence the rotational

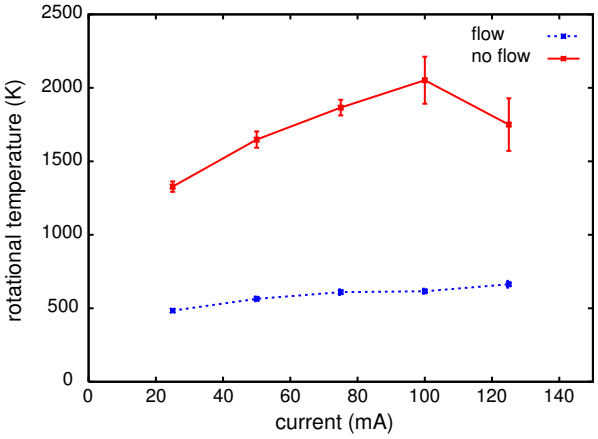

Figure 6.5: Rotational (gas) temperatures as a function of the discharge current in a Mach 2.85 supersonic flow at test section static pressure of 15 Torr. Error bars represent 95% confidence intervals.

lines are weak and the N_2 lines are not resolved well with the spectrometer used [49]. In the procedure used, the generated synthetic spectra at certain temperature are compared with measured spectra and the error between two spectra is calculated. The error is obtained by evaluating running-average of spectral line intensities near the wavelength of interest and it is represented as Eq. 4.15. The errors are evaluated at various temperatures and the temperature estimate is taken when error becomes minimum. Typical average error over a band is about 6 - 8 %. For the spectrum shown in Fig. 6.4, rotational temperatures are estimated as 430 K for the N_2^+ fit and 400 K for the N_2 fit, respectively. Note that the free stream temperature of the Mach 2.85 supersonic flow is about 110 K indicating that Joule (gas) heating of the flow is not negligible.

The estimates of rotational (gas) temperature at different currents are

presented in Fig. 6.5 at a fixed test section static pressure of 16 Torr. The solid line represents the temperature in the absence of flow and the dotted line in the presence of flow. The error bars represent 95% confidence intervals which are evaluated by assuming that statistical errors follow the Student t-distribution. The same error scheme will be used for temperature plots hereafter. The discharge structure is maintained in diffuse mode D for both cases. Currents beyond 125 mA are not included since the higher currents result in mixed mode M or constricted mode C discharge structures. In the absence of flow, temperatures are measured to be in the range of 1200-2000 K exhibiting a nearly monotonic increase with increasing current, except for the highest current of 125 mA, where the temperature drops slightly. In the presence of flow, the temperatures are much lower than a stagnant case, about 500 K, and show a slight increase with increasing current. The ambient gas temperature is at room temperature for cases without flow. For cases with supersonic flow, the free stream gas temperature drops significantly to about 110 K. Both the lower free stream temperature and convective effects in the flow explain the significantly lower gas temperatures of the discharge in the presence of flow. However, the temperature increase caused by the discharge is still five times larger than the free stream temperature in the presence of flow indicating a significant gas heating by the plasma.

Although rotational temperatures are nearly the same as the gas translational temperature, vibrational temperatures of molecular species can be significantly different from the translational temperature owing to much weaker

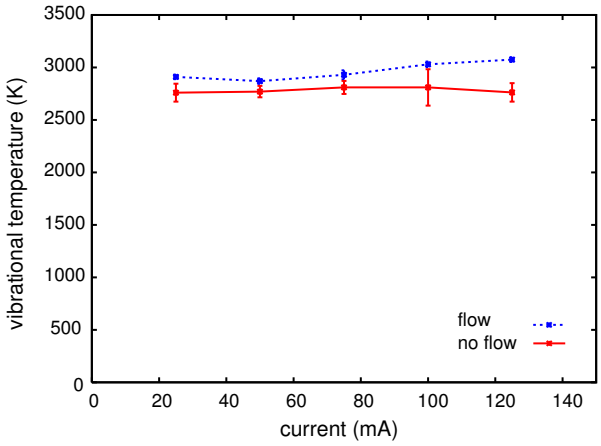

Figure 6.6: Measured vibrational temperature in the presence of a Mach 2.85 supersonic flow. The discharge conditions are the same as in Fig. 6.5. Error bars represent 95% confidence intervals.

vibrational-translational energy transfer. Once the rotational temperature is estimated by fitting the N_2 or N_2^+ rotational bands, band heads for (0-2), (1-3), and (2-4) vibrational transitions are matched by adjusting the vibrational temperature. Electronic moments and Frank-Condon factors for fitting different vibrational transitions are taken from the literature [52]. Figure 6.6 shows vibrational temperature profiles at different set-point currents. The solid line is for the case in the absence of flow and the dotted line is in the presence of supersonic flow. The test section pressures are set at 15 Torr to ensure that the discharge structures remain in the diffuse mode D discharge for both cases. Vibrational temperature estimates are about 2700 K for the no-flow case and slightly higher for the cases with the flow. Importantly, the vibrational temperatures are significantly higher than the rotational temperatures and the deviation becomes bigger in the presence of supersonic flow, which emphasizes

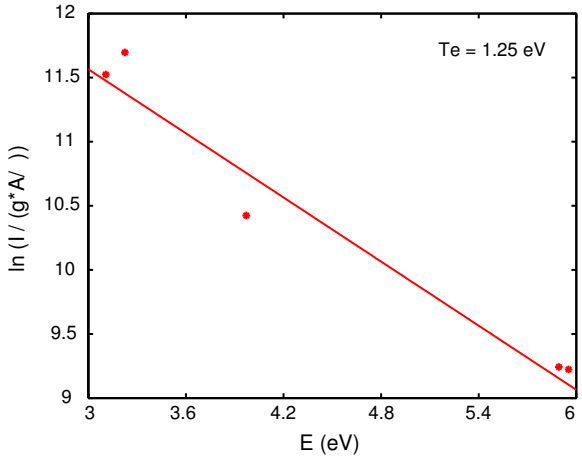

Figure 6.7: Boltzmann plot of Fe (I) emission lines for the estimation of electronic temperature.

the high degree of non-equilibrium of the discharge. This provides further evidence for the glow nature of the discharge. It can also be observed from Fig. 6.6 that the vibrational temperature, unlike the rotational temperature, remains almost constant with increasing current.

Electronic populations are assumed to be in equilibrium with a single characteristic electron temperature. In the constricted mode C discharge several atomic transition lines of Fe (I) are observed owing to erosion of the electrodes as shown in Fig. 4.5. These lines are used to estimate the electron temperature by making a linear fit to the Boltzmann plot as shown in the Fig. 6.7. The lowest electronic transitions are around 3 eV and the highest about 6 eV, providing a reasonable range of energies to characterize the electron energy distribution function. The electron temperature is found to be approximately 1.25 eV for all discharge conditions considered. The estimated electron tem-

perature for the discharge in this study is in the same range as those reported in the literature [64, 69]. Significant deviation of electron temperature from vibrational temperature again implies a highly non-equilibrium characteristic of the discharge in this study indicating again that the constricted mode C discharge is not an arc. In case of diffuse mode D discharges, the Fe (I) atomic lines are not distinguishable presumably owing to significantly reduced electrode erosion and hence electron temperature measurements are not possible with this technique.

6.1.3 Gas temperature profiles

In the previous chapter, it has been shown that flow actuation effects in a DC glow discharge are significant only when the discharge exists in the diffuse mode D and not in the constricted mode C. Since a flow actuation is produced by either gas heating or electrostatic forcing, it is useful to compare gas temperatures for both diffuse and constricted modes. Temperature measurements made just above the cathode for a constricted mode C discharge shows similar or slightly lower temperatures than the mode D discharge. Measurement just above the surface midway between the two electrodes, however, shows slightly higher temperatures compared to the region just above the cathode. Overall the peak rotational temperatures of mode D and mode C discharges are similar with each other. It is however important to note that despite similar gas temperatures the flow actuation effects are very different for the diffuse mode D discharge compared to the constricted mode C discharge. Two possible rea-

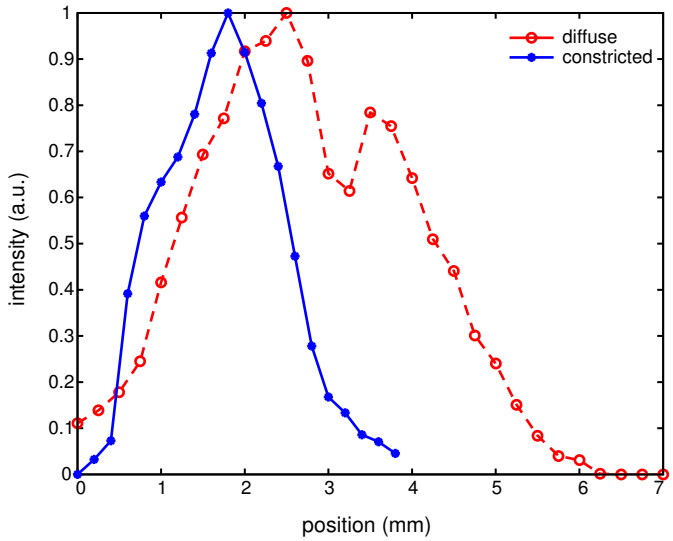

Figure 6.8: Spatial extent of spectral line intensity profile seen from the top. Dotted line is for a diffuse discharge and solid line is for a constricted discharge. A current input is 50 mA for both cases.

sons for this feature of the flow-plasma interaction are: 1) the spatial extent of the diffuse mode D discharge is larger than the constricted mode C discharge, which results in increased dilatational effects, and 2) electrostatic forcing plays an important role in the DC glow discharge induced flow actuation. To understand the gas heating effect in flow actuation of diffuse and constricted mode discharges despite similar gas temperature, spatially resolved measurements of emission intensity are used to estimate the spatial extent of the discharge. The spatial resolution of optical system is determined by magnification and fiber optic core diameter as presented in Sec. 3.4.

Figure 6.8 quantifies the extent of emissive region of surface discharge in a transverse direction (z-direction in Fig. 3.2) seen from top of the actuator

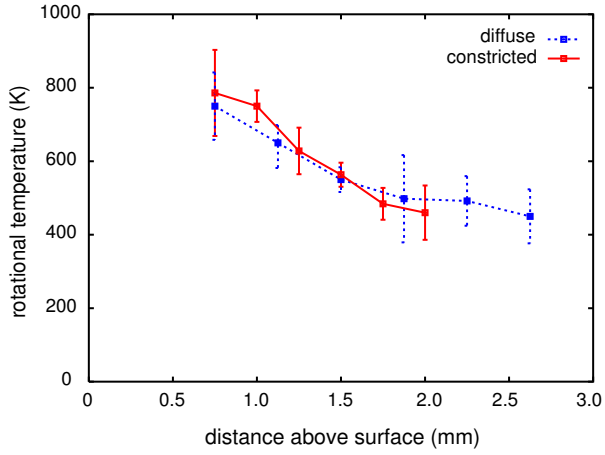

Figure 6.9: Measured rotational temperatures as a function of the transverse distance above the cathode in a Mach 2.85 supersonic flow. The free stream temperature is about 110 K. The pressures are 16 Torr for a diffuse mode D discharge and 30 Torr for a constricted C discharge. The set-point current is 50 mA for both cases. Error bars represent 95% confidence intervals.

(positive y). The ratio between diffuse and constricted is approximately two (1.8 mm and 3 mm FWHM for the constricted and the diffuse discharge, respectively). A similar ratio is obtained in a vertical direction (y-direction in Fig. 3.2) seen from side of the actuator (positive z). This suggests that the cross section of discharge luminous region is about 4 times larger for a diffuse discharge than a constricted discharge. However this luminosity profile does not directly explain the gas heating effect of two different discharge modes.

To provide insight into the volumetric extent of the gas heating, spatially resolved profiles of rotational temperatures are measured. Figure 6.9 shows the rotational temperature profiles for the diffuse mode D discharge and the constricted mode C discharge in the presence of the supersonic flow.

These temperatures are again obtained using the spectral fitting of measured emission spectra at different elevations (y direction; see Fig. 3.2). Note that the base elevation (0 mm) indicates where the spectral line intensity is detectable above the noise and this elevation is not necessarily the elevation of physical surface. Also the highest elevations for which temperature results are shown are the locations beyond which the spectral line intensities become too weak to estimate the temperature. The first data point is at 0.7 mm owing to the low signal below that elevation. The temperature is measured above cathode for the diffuse discharge and above the surface midway between the cathode and anode for the constricted discharge. The discharge current is set at 50 mA for both cases. The peak temperature occurs near the surface and is about 800 K for both modes. At greater elevations above the cathode the temperature drops to about 500 K at 2 mm for both modes. At elevations greater than 2 mm experimental data are not available for the constricted mode, but data for the diffuse mode indicate that the temperature would drop gradually for both modes. Overall, the results in Fig. 6.9 provide some insight into the dilatational effects due to gas heating in the diffuse mode and the constricted mode. Although the visible spatial extent of the discharge is very different for the diffuse mode and the constricted mode, the gas temperature profiles appear to be quite similar for the two modes. The similarity in the gas temperature spatial profiles provides some evidence that both the diffuse and the constricted modes produce similar dilatational effects on the flow. This implies that the flow actuation by DC surface discharge cannot be explained

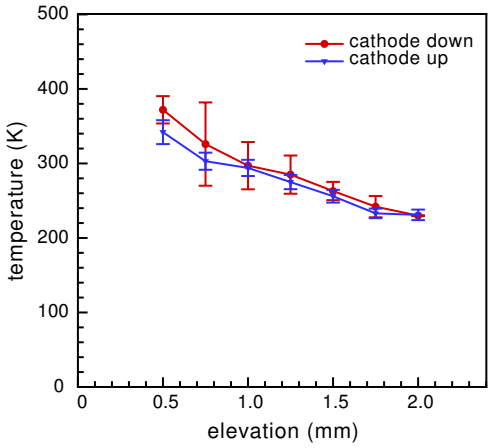

Figure 6.10: Measured rotational temperature profiles as a function of the transverse distance above the cathode in a Mach 2.85 supersonic flow. Both cathode downstream and cathode upstream cases are shown. The free stream temperature is about 110 K. The pressures are 16 Torr and the set-point current is 50 mA for both cases. Error bars represent 95% confidence intervals.

by gas heating effect alone.

It is also shown that the actuation becomes weaker when the electrode polarity is switched from cathode upstream to cathode downstream. The rotational temperature profiles for cathode downstream case are compared with cathode upstream case. Figure 6.10 presents the spatial profiles of rotational temperature for cathode downstream and cathode upstream cases. Corresponding schlieren images are presented in Fig 5.13. As shown in Fig. 6.10, the peak rotational temperature and spatial profiles above the cathode are similar to each other. This indicates the gas heating effects are also similar to each other but flow actuation is not the same in the two cases as shown before. In addition to the results of spatial profiles of diffuse and constricted

discharge cases, this result again suggests that the electrostatic forcing plays an important role in supersonic flow actuation.

6.2 Electrohydrodynamic (EHD) effect by DC surface discharge

As shown in the previous section, significant gas heating is evident from the spectroscopic results, which suggests that dilatational effects play an important role in flow actuation. The fact that both diffuse mode D and constricted mode C discharges (Fig. 6.9) as well as both cathode upstream and cathode downstream cases (Fig. 6.10) have similar gas temperature spatial profiles implies that dilatational effects on the flow are similar at a given discharge power. The dilatational effect due to gas heating is essentially an isotropic phenomenon that causes a local high pressure zone which imitates the presence of a surface bump. Consequently, if dilatation is the only mechanism by which plasma-flow actuation occurs then one would expect the emergence of a weak shock from the discharge zone for constricted mode and cathode downstream case. However, the complete absence of any detectable flow actuation in the constricted mode C discharge and weaker actuation in cathode downstream case suggest the possible importance of electrostatic forcing as an additional mechanism that influences the overall supersonic flow actuation phenomena.

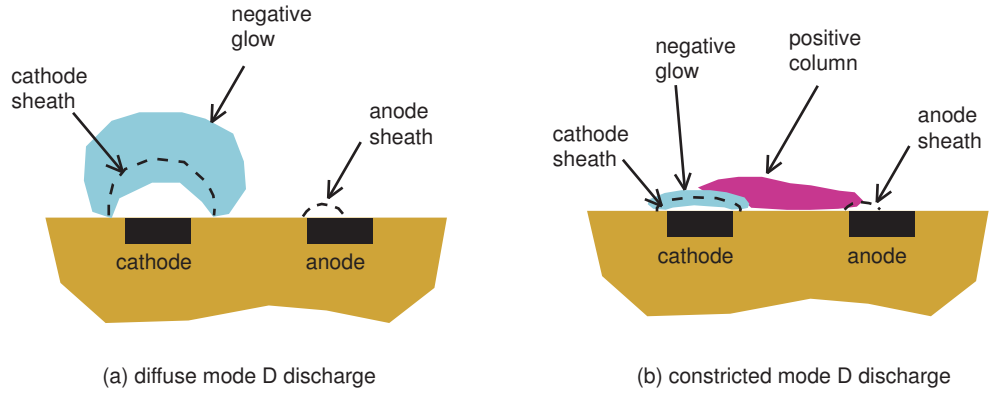

Figure 6.11: Detailed structures of DC surface discharges in diffuse mode D (a) and constricted mode C (b). Cathode sheath thickness is exaggerated.

6.2.1 EHD force in DC surface discharge

To study the EHD effect of DC surface discharges, detailed structures of the discharge need to be explored. Figure 6.11 illustrates detailed structures of diffuse mode D and constricted mode C discharges. As already been discussed in Sec. 5.3, the discharge luminous region (negative glow) for diffuse discharge is bigger than constricted discharge. This is primarily because of the larger cathode sheath thickness in diffuse mode. In the cathode sheath, the plasma is non-neutral where ion population is much larger than electron population. However, between electrodes, the plasma is quasi-neutral. Net EHD force produced in these two regions is illustrated in Fig. 6.12. In cathode sheath region (Fig. 6.12(a)), most ions collide with neutrals as they approach to the cathode and transfer momentum to neutral particles. Resultant EHD force is greater than zero owing to the larger population of ions. It is also expected that EHD forcing region is bigger with the larger cathode sheath thickness.

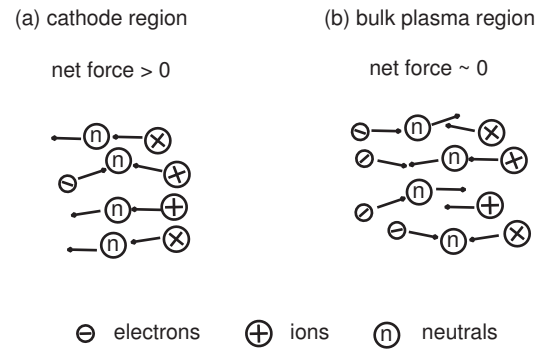

Figure 6.12: Schematics of EHD forcing in cathode region (a) and bulk plasma region (b).

But in bulk plasma region between electrodes (Fig. 6.12(b)), net EHD force produced by ions and electrons is close to zero. The force exerted to neutrals by electrons (F_{en}) are nearly the same as the force exerted by ions (F_{in}) as follows.

$$F_{en} = M_{en} n_e \nu_e u_e \tag{6.1a}$$

$$F_{in} = M_{in} n_i \nu_i u_i, , \tag{6.1b}$$

where M_{en} and M_{in} are reduced mass of electron-neutral pair and ion-neutral pair, ν_e and ν_i are collision frequency of electrons and ions with respect to neutrals, u_e and u_i are drift velocity of electrons and ions. Here, $u_e = \mu_e E = \frac{e}{M_{en}\nu_e} E$ and $u_i = \mu_i E = \frac{e}{M_{in}\nu_i} E$, where μ_e and μ_i are the mobility of electrons and ions, E is electric field, e is unit charge. Putting u_e and u_i into Eqs. 6.1a and 6.1b makes

$$F_{en} = e n_e E \tag{6.1c}$$

$$F_{in} = e n_i E. \tag{6.1d}$$

Since the number densities of electrons and ions are similar in bulk region, $F_{en} \approx F_{in}$. Consequently, EHD effect in the bulk plasma region is expected to be negligible. The magnitude of EHD force in the cathode sheath region will be discussed in the following sections.

6.2.2 Estimation of EHD effect

To understand electrostatic forcing in the cathode sheath, a rough analytical estimate of electrostatic forcing in the cathode sheath is obtained for both diffuse mode D and constricted mode C discharge using a collisional cathode sheath theory. It is expected that the cathode directed drift motion of positive ions in the sheath causes a compression of the gas within the sheath and a corresponding expansion of the gas above the sheath. It is also expected that the pressure increase within the sheath and expansion outside it are a significant fraction of the total pressure. We assume a one-dimensional, planar, collisional DC sheath for simplicity and assume the Child's law sheath approximation of large cathode potential fall to be valid [61]. This approximation precludes the presence of all negatively charged particles in the sheath and only positive ions are accelerated through the cathode potential drop by mobility limited ion transport. A detailed derivation is provided in Appendix A.

Considering typical operating conditions, we can now make an estimate of the ion pressure (gas compression in the sheath) for both the diffuse mode D and constricted mode C discharges. A pressure of 16 Torr with an ion mobility of 9×10^{-3} m^2/V-s (N_2^+ ion drifting in N_2) is assumed for both cases. For a

diffuse mode D with low current, say $I = 50$ mA ($J = 1.1 \times 10^4$ A/m^2) and a high cathode sheath voltage drop of $V_c = 1000$ V, the sheath thickness is predicted to be about 0.2 mm and the ion pressure rise is about 245 Pa (about 1.84 Torr). On the other hand, for constricted mode C, with a higher current of say $I = 300$ mA ($J = 6.7 \times 10^4$ A/m^2) and a lower sheath voltage drop of $V_c = 300$ V, the sheath thickness is about 0.05 mm and the ion pressure rise is about 367 Pa (2.76 Torr) from Eq. A.10. Clearly, the ion pressure rises and in turn the gas pressure rise in the sheath in both the diffuse and constricted modes is comparable to the total pressure of 16 Torr. The pressure rise however occurs in a much smaller cathode sheath thickness in the constricted case compared to the diffuse case.

The above estimates of equivalent forcing in the cathode sheath is obtained regardless of the presence of supersonic flow. For the electrostatic forcing effect to be substantial in supersonic flow, the work done by pressure force induced by the discharge must be a significant portion of the work done by bulk flow. This can be evaluated by a non-dimensional number called 'EHD interaction parameter (I_{EHD})'. This parameter compares the Coulomb force work with flow kinetic energy. The derivation and estimates of I_{EHD} are presented in Appendix B. As presented in the calculation, when I_{EHD} is evaluated in the free stream (Eq. B.1), the electrostatic forcing is only about 1% of flow kinetic force at typical operating conditions. However when I_{EHD} is evaluated in the boundary layer (Eq. B.5) where bulk flow velocity is much slower than free stream velocity, the electrostatic forcing effect becomes comparable to flow

kinetic force. This implies that the electrostatic forcing can play a role inside a supersonic flow boundary layer.

6.2.3 Induced flow by EHD effect

The importance of electrostatic forcing based on the above estimation is now demonstrated experimentally in a stagnant chamber described in Sec. 3.5. Because direct evaluation of electrostatic forcing effect in supersonic flow is not practically possible, the DC surface discharge actuator is tested in a stagnant environment. Also, the pressure is set to one atmosphere partly because PIV technique fails to find correct velocity correlations at low seed density at low pressures. The primary measure of the electrostatic forcing effect is the magnitude of induced flow velocity. PIV measurements provide a reasonably accurate velocity contour of induced flow field near the discharge region provided the seed density is qualitatively high.

Figure 6.13 shows an velocity contour plot of the induced flow produced by DC surface discharge at a discharge current of 26 mA and a voltage drop of 1 kV. A pair of pin-like electrodes is turned on. Due to a high pressure condition, the discharge structure resembles a constricted discharge shown in Fig. 5.4 (c). The vector field in Fig. 6.13 shows that a neutral gas is dragged towards the cathode from the anode region and maximum acceleration occurs right next to the cathode region. Downward motion near the cathode is caused by the current lines directed to the electrode. As the induced flow passes away from the cathode, the flow slows down and experiences retardation

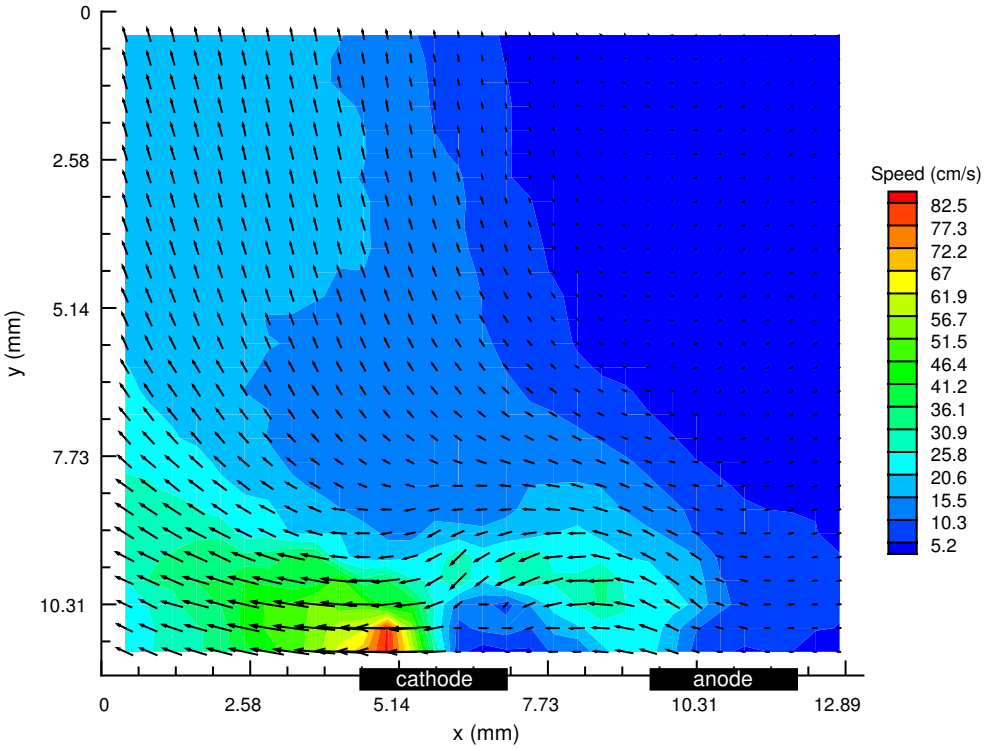

Figure 6.13: Vector contour plot of plasma-induced flow field. The discharge current is 26 mA and the pressure is one atmosphere.

resulting in upward-directed motion due to the momentum deficit as well as gas and surface heating by the plasma. The factors that influence the motion of particles are background gas density, gravity, particle charging, buoyancy and so on. Gravity is usually bigger than buoyancy except when there is perceptible heating. The particle motion that is described above clearly indicates that the charging of the seed particles does not play a big role because particles are primarily negatively charged [70] and negatively charged particles levitate near the sheath edge [71].

The figure clearly indicates that the electrostatic forcing in DC surface discharge can induce a bulk flow in stagnant air. The maximum induced velocity is measured to be as high as about 1 m/s near the cathode. Since the discharge conditions are not similar as the supersonic flow conditions, the contribution of this electrostatic forcing in supersonic flow actuation is expected to be different from high pressure results shown here. However, the order of 1 m/s flow actuation is not negligible especially because the actuation occur in the boundary layer. Note that the friction velocity in the Mach 2.85 supersonic flow boundary layer is estimated as about 28 m/s (see Appendix B). Along with the above estimate of electrostatic forcing, the induced flow study provides the preliminary insight into the potential role of electrostatic forcing which is commonly neglected by most researches as an important mechanism for supersonic flow actuation.

Figure 6.14 illustrates the role of electrostatic forcing in supersonic flow inferred from the above estimates and experimental results. Left column (Figs. 6.14(a) and (c)) depicts diffuse mode D discharge and right column (Figs. 6.14(b) and (d)) depicts constricted mode C discharge. When only gas heating is considered, the actuation effects by two modes are similar as presented in Fig. 6.9 and the streamlines deflect a little bit away from the surface as shown in top images (Figs. 6.14(a) and (b)). When EHD force is also considered in addition to gas heating effect, the supersonic flow in diffuse mode D discharge experiences larger area of electrostatic forcing and hence the streamline deflects further (Figs. 6.14(a) $\rightarrow$ (c)) resulting in the generation of weak

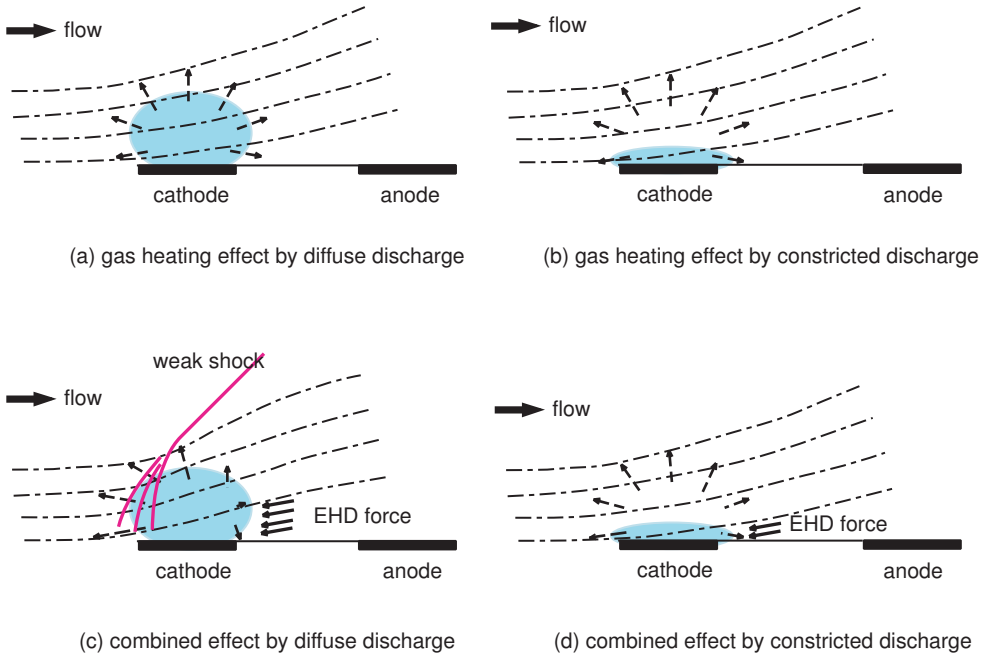

Figure 6.14: Illustration of gas heating effect and EHD effect on supersonic flow in diffuse mode D discharge (left column) and constricted mode C discharge (right column). Top images show the effect of gas heating alone and bottom images show the combined effect and corresponding on set of weak oblique shock. Dotted arrows indicate the resultant force and solid arrows indicate EHD force. Dotted-dash lines are streamlines.

oblique shock. However, in constricted discharge, the region of EHD forcing is very thin and hence the resultant force is not big enough to deflect the streamlines further (Figs. 6.14(b) $\rightarrow$ (d)). The effect of switching the electrode polarity is also explained in the same way as shown in Fig. 6.15. Assuming the discharges are in diffuse mode D or mixed mode M and hence the EHD forcing is effective, when the cathode is located downstream, EHD force produces favorable pressure gradient. Therefore, the streamlines get flatten and the disturbance becomes weaker. The above explanation is now consistent with

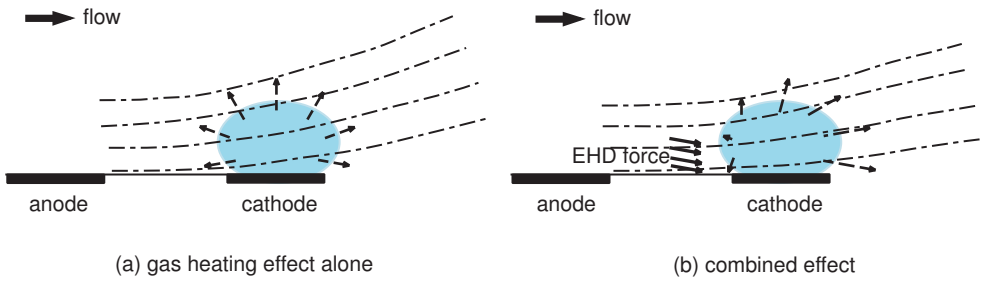

Figure 6.15: Illustration of gas heating effect and EHD effect on supersonic flow in cathode upstream location (a) and cathode downstream location (b). Dotted arrows indicate the resultant force and solid arrows indicate EHD force. Dotted-dash lines are streamlines.

experimental results presented in the previous chapter where diffuse mode D discharge produced a weak oblique shock while constricted mode C discharge produced no discernable shock. Also the disturbance becomes weaker as the electrode polarity was switched to cathode downstream location. More detailed explanation of EHD forcing effect than presented in this study needs to be accompanied with further experimental efforts and numerical studies.

Chapter 7

Conclusions

DC surface discharge plasmas were studied for the supersonic flow actuation. DC glow plasma discharges were generated with pin-like electrodes in the presence of a Mach 2.85 supersonic flow. Different discharge structures like diffuse (mode D), constricted (mode C), and mixed (mode M) were observed and these modes exhibit different interactions with the oncoming supersonic flow. The diffuse mode D discharge is produced when the discharge currents and test section pressures are low. Higher currents ($>\sim$150 mA) and higher pressures ($>\sim$25 Torr) drive the diffuse discharge into the constricted mode C discharge. The particular power supply we are using (current controlled) causes a bistable mixed mode at intermediate currents and pressures, where the discharge switches rapidly between the diffuse and constricted modes. In mode D, only the cathode layer with the negative glow is visible, whereas in mode C the positive column is also visible. Visible flow actuation was obtained for discharges in the diffuse mode D, as evidenced by the emergence of a weak oblique shock originating from the cathode location on the surface. No such actuation was observed in the case of the constricted mode C discharge. High-speed laser schlieren imaging confirmed that plasma actuation of the flow was achieved at high bandwidth ($\sim$100 μs or less actuation response

time). Rotational, vibrational and electronic temperatures in the discharges were estimated by using optical emission spectroscopy. N_2^+ first negative and N_2 second positive rovibronic band systems were observed in both diffuse and constricted discharges. A significant decrease in the intensity of the N_2^+ system was observed in the positive column with constricted discharges, whereas the N_2 system was detected over entire discharge volume. The rotational and vibrational temperature estimates were obtained by fitting synthetic spectra to the measured one. Gas temperatures (assumed to be equal to the N_2 and N_2^+ rotational temperatures) in the diffuse discharge in the absence of a flow were estimated to be around 1200 K - 2000 K at set point currents of 25 mA - 125 mA. In the presence of supersonic flow, gas temperature drops to near 500 K remaining almost constant with increasing currents. Vibrational temperatures were measured to be as high as 3000 K, which is significantly higher than the rotational temperatures. Electronic temperature was found to be as high as 1.25 eV by Boltzmann fitting of Fe (I) atomic lines. The electronic temperature could only be estimated for the constricted mode because mode D discharge did not produce sufficient emission from Fe (I). The disparate rotational, vibrational, and electronic temperatures confirm that both the diffuse and constricted mode discharges are non-equilibrium glow discharges and not arcs. Spatially-resolved gas temperature above the cathode surface shown very similar temperature profiles for the diffuse and constricted mode discharges resulting in very similar dilatational forcing effects for both discharge modes. Finally, the role of electrostatic forcing in supersonic flow actuation was stud-

ied analytically and experimentally. A analytical model for collisional cathode sheaths confirmed that significant gas pressure increases (compression) were obtained for both diffuse and constricted modes within the sheath. However, the cathode sheath thickness for the constricted mode was much smaller than the diffuse mode discharge. The compression within the sheath must be accompanied by a corresponding expansion outside the sheath which can partially or fully negate the dilatational effect due to gas heating. It is speculated that in the constricted case the expansion above the sheath almost completely negates the dilatational forcing resulting in the absence of a shock emerging from the discharge zone. The evidence of electrostatic forcing was confirmed by PIV measurement of plasma-induced flow field in a stagnant air environment. The induced flow velocity reached about 1 m/s implying that the electrostatic forcing can play an important role in supersonic flow boundary layer where bulk flow velocity is much slower than free stream velocity.

Appendices

Appendix A

Estimation of ion pressure in the sheath

First calculate typical values of plasma properties.

$$\text{Background density,} \quad n_g = \frac{P}{kT} \tag{A.1}$$
$$= \frac{16/760 * 101325}{1.3807 \times 10^{-23} \cdot 500} = 3.09 \times 10^{23} m^{-3}$$
$$\text{Mean free path,} \quad \lambda_i = \frac{1}{n_g \sigma_i} \tag{A.2}$$
$$= \frac{1}{2.9 \times 10^{23} \cdot 7.07 \times 10^{-20}} = 11.4 \mu m$$
$$\text{Debye length,} \quad \lambda_{Debye} = 743\sqrt{\frac{T_e}{n_e}} = 58.7 \mu m \tag{A.3}$$

Ions are dominant in the cathode sheath compared to the electrons due to a steep potential drop across sheath. Owing to the acceleration of ions in the sheath, ion pressure drops as it approaches to the cathode. Assuming electrons are absent in the cathode sheath, ion population is governed by ion continuity as,

$$n_i u_i = n_s u_s$$
$$n_i = n_s \frac{u_s}{u_i} \tag{A.4}$$

where n_s and u_s are ion number density and ion velocity at the sheath edge, respectively. Here, ionization in the sheath and the contribution of secondary

electron emission to the total discharge current are neglected. At the sheath edge, current density $J_o = en_s u_s$. Hence, ion population in the cathode sheath becomes,

$$n_i = \frac{J_o}{eu_i} = \frac{J_o}{e\mu_i E}. \tag{A.5}$$

Here, ion drift velocity is assumed mobility limited (i.e. $u_i = \mu_i E$).

Poisson equation describes the relation between electric field and space charge density as,

$$\varepsilon_o \nabla \cdot E = \rho = en_i \tag{A.6}$$

and one-dimensional form gives

$$\frac{dE}{dy} = \frac{e}{\varepsilon_o} n_i = \frac{J_o}{\varepsilon_o \mu_i E}, \tag{A.7}$$

where y is defined in the direction perpendicular to the electrode surface and the sheath edge plane, with $y = 0$ located at the sheath edge. Integrating once and assuming the electric field at the sheath edge is zero, we obtain an expression for the sheath electric field as

$$E = \sqrt{\frac{2J_o}{\varepsilon_o \mu_i} y}. \tag{A.8}$$

Integrating again with $E = -dV/dy$, we get an expression for the sheath thickness

$$t_s = \left(\frac{\varepsilon_o \mu_i}{2J_o}\right)^{\frac{1}{3}} \left(\frac{3V_c}{2}\right)^{\frac{2}{3}}, \tag{A.9}$$

which is a function of the cathode voltage drop V_c, the ion mobility, and the current density.

Since mean free path (11.4μ m) is much smaller than expected sheath thickness (about 1 mm), sheath is expected to be collisional and hence ion pressure force is balanced with electrostatic force. Using the dominant terms in the ion momentum equation in the collisional sheath (ion pressure gradient and the electrostatic force), i.e.$\nabla P_i = en_iE$, the total ion pressure rise across the sheath is estimated as

$$\Delta P_i = \frac{J_o}{\mu_i} t_s. \tag{A.10}$$

At typical discharge conditions, the current densities (J_o) are $\frac{50\times10^{-3}}{\frac{\pi}{4}0.0024^2} = 1.1 \times 10^4$ A/m^2 in diffuse mode and $\frac{300\times10^{-3}}{\frac{\pi}{4}0.0024^2} = 6.7 \times 10^4$ A/m^2 in constricted mode. With an ion mobility of 9×10^{-3} m^2/V-s (N_2^+ ion drifting in N_2) and V_c = 1000 V and 300 V in diffuse mode and constricted mode, respectively, the ion pressure rise is about 245 Pa in diffuse mode and about 367 Pa in constricted mode.

Appendix B

EHD interaction parameter

It is important to quantify the magnitude of the plasma flow actuation effect. For the electrostatic forcing, EHD interaction parameter (I_{EHD}) provides a qualitative measure of effectiveness of electrostatic forcing on the flow. This parameter compares the Coulomb force work and flow kinetic energy. The Coulomb force work can be equivalent to ion pressure work in the cathode sheath as presented in Appendix A and flow kinetic energy can be represented as dynamic pressure ρu^2, which give the I_{EHD} as,

$$I_{EHD} = \frac{\Delta P}{\rho u^2} \tag{B.1}$$

In Ref. [30], Macheret *et al.* showed that I_{EHD} can be estimated as,

$$I_{EHD} = \frac{\Delta P}{\rho u^2} = \frac{e n_+ \Delta\varphi}{\rho u_\infty^2} = \frac{\varepsilon_o E^2}{\rho u_\infty^2} \tag{B.2}$$

In Ref. [11], authors suggested that the velocity should be evaluated in the boundary layer, which means ρu_∞^2 should be replaced with ρu^{*2} where u^* represents friction velocity. By definition,

$$u^* = \sqrt{\frac{\tau_w}{\rho}} = u_\infty \sqrt{\frac{C_f}{2}} \tag{B.3}$$

In turbulent flow, the friction coefficient (C_f) follows the empirical law as,

$$C_f = 0.027 Re_x^{-\frac{1}{7}} \tag{B.4}$$

where Re_x is a local Reynolds number. Hence, I_{EHD} becomes,

$$I_{EHD} = \frac{74.07 Re_x^{\frac{1}{7}} \Delta P}{\rho u_\infty^2} \tag{B.5}$$

However, the density (ρ) in dynamic pressure term should be also evaluated in the boundary layer. This makes I_{EHD} as,

$$I_{EHD} = \frac{\Delta P}{\rho_w u^{*2}} = \frac{R T_w \Delta P}{P_w u^{*2}} \tag{B.6}$$

where R is a gas constant, $P_w = P_\infty$, and T_w is a recovery temperature which is a room temperature in this case. Hence, I_{EHD} becomes,

$$I_{EHD} = \frac{74.07 R T_w Re_x^{\frac{1}{7}} \Delta P}{P_\infty u_\infty^2} \tag{B.7}$$

ΔP can be evaluated from Eq. A.10.

Under typical operating conditions provided in Table B.1, I_{EHD}'s are;

from Eq. B.1 $---$ 0.01

from Eq. B.5 $---$ 4.8

from Eq. B.7 $---$ 12.6

As shown in the above estimates, electrostatic forcing cannot be neglected especially if the forcing occurs within the boundary layer.

Table B.1: Typical operating condition

parameter	values
M	2.85
T_o	300 K
P_o	468 Torr
x location	15 cm
u_∞	610.8 m/s
ρ_∞	0.064942 kg/m^3
P_∞	2130.5 Pa
T_∞	114.3 K
Re_x	4.41×10^5
C_f	0.00421747
u^*	28.04 m/s
ρ_w	0.024744 kg/m^3

Bibliography

[1] J. P. Boeuf. Plasma display panels: physics, recent developments and key issues. *J. Phys. D: Appl. Phys.*, 36(6):R53–79, 2003.

[2] C. L. Enloe, T. E. McLaughlin, R. D. VanDyken, K. D. Kachner, E. J. Jumper, and T. C. Corke. Mechanisms and responses of a single dielectric barrier plasma actuator: Plasma morphology. *AIAA Journal*, 42(3):589–594, 2004.

[3] J. R. Roth. Aerodynamic flow acceleration using paraelectric and peristaltic electrohydrodynamic effects of a one atmosphere uniform glow discharge plasma. *Phys. of Plasmas*, 10(5):2117–2126, 2003.

[4] M. Bolitho and J. D. Jacob. Use of aggregate plasma synthetic jet actuators for flow control. volume AIAA-2007-637 of *45th AIAA Aerospace Sciences Meeting and Exhibit*, January 2007.

[5] J. Menart, J. Shang, R. Kimmel, and J. Hayes. Effects of magnetic fields on plasmas generated in a Mach 5 wind tunnel. volume AIAA-2003-4165 of *34th AIAA Plasmadynamics and Lasers Conference*, June 2003.

[6] R. L. Kimmel, J. R. Hayes, J. A. Menart, and J. Shang. Effect of surface plasma discharges on boundary layers at Mach 5. volume AIAA-2004-509 of *42nd AIAA Aerospace Sciences Meeting and Exhibit*, January 2004.

[7] J. S. Shang, J. Menart, R. Kimmel, and J. Hayes. Hypersonic inlet with plasma induced compression. volume AIAA-2006-764 of *44th AIAA Aerospace Sciences Meeting and Exhibit*, January 2006.

[8] S. Leonov, V. Bityurin, K. Savelkin, and D. Yarantsev. Effect of electrical discharge on separation processes and shocks position in supersonic airflow. volume AIAA-2002-0355 of *40th AIAA Aerospace Sciences Meeting and Exhibit*, January 2002.

[9] S. B. Leonov and D. A. Yarantsev. Mechanisms of flow control by near-surface electrical discharge generation. volume AIAA-2005-780 of *43rd AIAA Aerospace Sciences Meeting and Exhibit*, January 2005.

[10] J. Menart, M. McFarland, and K. Campbell. Use of a plasma arc to produce large surface pressure changes on a flat plate in a Mach 5 flow. volume AIAA-2007-631 of *45th AIAA Aerospace Sciences Meeting and Exhibit*, January 2007.

[11] Y. G. Utkin, S. Keshav, J. H. Kim, J. Kastner, I. V. Adamovich, and M. Samimy. Development and use of localized arc filament plasma actuators for high-speed flow control. *J. Phys. D: Appl. Phys.*, 40:685–694, 2007.

[12] S. Merriman, E. Plönjes, P. Palm, and I. Admovich. Shock wave control by nonequilibrium plasmas in cold supersonic gas flows. *AIAA Journal*, 39:1547–1552, 2001.

[13] W. Shyy, G. Jayaraman, and A. Andersson. Modeling of glow discharge-induced fluid dynamics. *J. Appl. Phys.*, 92(11):6434–6443, 2002.

[14] F. Massines, A. Rahebi, P. Decomps, R. Ben Gadri, P. Segur, and C. Mayoux. Experimental and theoretical study of a glow discharge at atmospheric pressure controlled by dielectric barrier. *J. Appl. Phys.*, 83(6):2950–2957, 1988.

[15] J. Shin and L. L. Raja. Dynamics of pulse phenomena in helium dielectric-barrier atmospheric-pressure glow discharges. *J. Appl. Phys.*, 94(12):7408–7415, 2003.

[16] X. Yuan, J. Shin, and L. L. Raja. One-dimensional simulation of multi pulse phenomena in dielectric-barrier atmospheric-pressure glow discharges. *Vacuum*, 80(11-12):1199–1205, 2006.

[17] S. Pavon, J-L Dorier, Ch. Hollenstein, P. Ott, and P. Leyland. Effects of high-speed airflows on a surface dielectric barrier discharge. *J. Phys. D: Appl. Phys.*, 40:1733–1741, 2007.

[18] J. Menart, S. Stanfield, J. Shang, R. Kimmel, and J. Hayes. Study of plasma elecrode arrangements for optimum lift in a Mach 5 flow. volume AIAA-2006-1172 of *44th AIAA Aerospace Sciences Meeting and Exhibit*, January 2006.

[19] Yu. P. Raizer. *Gas Discharge Physics*. Springer, New York, 1991.

[20] R. Yano, V. Contini, E. Plönjes, P. Plam, S. Merriman, S. Aithal, I. Adamovich, W. Lempert, V. Subramaniam, and J. W. Rich. Supersonic nonequilibrium plasma wind-tunnel measurements of shock modification and flow visualization. *AIAA Journal*, 38(10):1879–1888, 2000.

[21] G. Faure and S. M. Shkol'nik. Determination of rotational and vibrational temperatures in a discharge with liquid non-metallic electrodes in air at atmospheric pressure. *J. Phys. D: Appl. Phys.*, 31(10):1212–1218, 1998.

[22] J. M. Williamson and C. A. DeJoseph Jr. Determination of gas temperature in an open-air atmospheric pressure plasma torch from resolved plasma emission. *J. Appl. Phys.*, 93(4):1893–1898, 2003.

[23] A. Chelouah, E. Marode, G. Hartmann, and S. Achat. A new method for temperature evaluation in a nitrogen discharge. *J. Phys. D: Appl. Phys.*, 27:940–945, 1994.

[24] S. A. Stanfield, J. Menart, J. Shang, R. L. Kimmel, and J. R. Hayes. Application of a spectroscopic measuring technique to plasma discharge in hypersonic flow. volume AIAA-2006-559 of *44th AIAA Aerospace Sciences Meeting and Exhibit*, January 2006.

[25] D. H. Oza, R. L. Greene, and D. E. Kelleher. Collisional broadening of the Balmer-α transition of H and He^+ in plasmas. *Phys. Rev. A*, 37(2):531–536, 1988.

[26] J. Ashkenazy, R. Kipper, and M. Caner. Spectroscopic measurements of electron density of capillary plasma based on stark broadening of hydrogen lines. *Phys. Rev. A*, 43(10):5568–5574, 1991.

[27] V. Milosavljevic and S. Djenize. The He I 706.52 nm line shape characteristics in the plasma diagnostics. *Eur. Phys. J. D.*, 23:385–390, 2003.

[28] C. O. Laux, T. G. Spence, C. H. Kruger, and R. N. Zare. Optical disgnostics of atmospheric pressure air plasmas. *Plasma Sources Sci. Technol.*, 12:125–138, 2003.

[29] Y. G. Utkin, S. Keshav, J. H. Kim, J. Kastner, I. V. Adamovich, and M. Samimy. Characterization of localized arc filament plasma actuators used for high-speed flow control. volume AIAA-2007-787 of *45th AIAA Aerospace Sciences Meeting and Exhibit*, January 2007.

[30] S. O. Macheret, M. N. Shneider, and R. B. Miles. Magnetohydrodynamic and electrohydrodynamic control of hypersonic flows of weakly ionized plasmas. *AIAA Journal*, 42(7):1278–1387, 2004.

[31] E. Menier, L. Leger, E. Depussay, V. Lago, and G. Artana. Effect of a dc discharge on the supersonic rarefied air flow over a flat plate. *J. Phy. D: Appl. Phys.*, 40(3):695–701, 2007.

[32] S. Kanazawa, M. Kogoma, T. Moriwaki, and S. Okazaki. Stable glow plasma at atmospheric pressure. *J. Phys. D: Appl. Phys.*, 21:838–840,

1988.

[33] Y. B. Golubovskii, V. A. Maiorov, J. F. Behnke, J. Tepper, and M. Lindmayer. Study of the homogeneous glow-like discharge in nitrogen at atmospheric pressure. *J. Phys. D: Appl. Phys.*, 37:1346–1356, 2004.

[34] X. Yuan and L. L. Raja. Computational study of capacitively coupled high-pressure glow discharges in helium. *IEEE Trans. on Plasma Sci.*, 31:495–503, 2003.

[35] J. Shin and L. L. Raja. Run-to-run variations, asymmetric pulses, and long time-scale transient phenomena in dielectric-barrier atmospheric pressure glow discharges. *J. of Phys. D: Appl. Phys.*, 40:3145–3154, 2007.

[36] C. L. Enloe, T. E. McLaughlin, R. D. VanDyken, K. D. Kachner, E. J. Jumper, T. C. Corke, M. Post, and O. Haddad. Mechanisms and responses of a single dielectric barrier plasma actuator: Geometric effects. *AIAA Journal*, 42:595–604, 2004.

[37] M. L. Post and T. C. Corke. Separation control on high angle of attack airfoil using plasma actuators. *AIAA Journal*, 42:2177–2184, 2004.

[38] J. Huang, T. C. Corke, and F. O. Thomas. Plasma actuators for separation control of low-pressure turbine blades. *AIAA Journal*, 44(1):51–57, 2006.

[39] T. Segawa, H. Furutani, and H. Yoshida. Wall normal jet under elevated temperatures produced by surface plasma actuator. volume AIAA-2007-784 of *45th AIAA Aerospace Sciences Meeting and Exhibit*, January 2007.

[40] De Seversky. Ionocraft, Apr. 1964. U.S. Patent 3,130,945.

[41] F. Grange, N. Soulem, J. F. Loiseau, and N. Spyrou. Numerical and experimental determination of ionizing front velocity in a DC point-to-plane corona discharge. *J. Phys. D: Appl. Phys.*, 28(8):1619–1629, 1995.

[42] R. Peyrous and R. M. Millot. Ozone generationo in oxygen by corona discharges in a point-to-plane gap subjected to a chopped DC positive voltage. *J. Phys. D: Appl. Phys.*, 14(12):2237–2242, 1981.

[43] L. Leger, E. Moreau, and G. G. Touchard. Effect of a dc corona electrical discharge on the airflow along a flat plate. *IEEE Trans. Ind. Appl.*, 38(6):1478–1485, 2002.

[44] J. Menart, S. Handerson, C. Atzbach, J. Shang, R. L. Kimmel, and J. R. Hayes. Study of surface and volumetric heating effects in a Mach 5 flow. volume AIAA-2004-2262 of *35th AIAA Plasmadynamics and Lasers Conference*, June-July 2004.

[45] R. Meyer, M. Nishihara, A. Hicks, N. Chintala, M. Cundy, W. R. Lempert, I. V. Adamovich, and S. Gogineni. Measurements of flow conductivity and density fluctuations in supersonic nonequilibrium magnetohydrodynamic flows. *AIAA Journal*, 43:1923–1929, 2005.

[46] S. B. Leonov, V. A. Bityurin, D. A. Yarantsev, Y. I. Isaenkov, and V. R. Soloviev. High-speed flow control due to interaction with electrical discharges. volume AIAA-2005-3287 of *AIAA/CIRA 13th International Space Planes and Hypersonics Systems and Technologies*, January 2005.

[47] E. R. Lachney. Two-dimensional temperature and pressure imaging of a supersonic flat plate wake. Master's thesis, The University of Texas at Austin, May 1995.

[48] M. Raffel, C. Willert, and J. Kompenhans. *Particle Image Velocimetry: A Practical Guide*. Springer, Germany, 1998.

[49] J. M. Williamson, P. Bletzinger, and B. N. Ganguly. Gas temperature determination in a N_2/Ar dielectric barrier discharge by diode-laser absorption spectroscopy and resolved plasma emission. *J. Phys. D: Appl. Phys.*, 37(12):1658–1663, 2004.

[50] G. Hartmann and P. C. Johnson. Measurements of relative transition probabilities and the variation of the electronic transition moment for N_2 $C^3\Pi_u$ - $B^3\Pi_g$ second positive system. *J. Phys. B: Atom. Molec. Phys.*, 11(9):1597–1611, 1978.

[51] H. Nassar, S. Pellerin, K. Musiol, O. Martinie, N. Pellerin, and J. M. Cormier. N_2^+/N_2 ratio and temperature measurements based on the first negative N_2^+ and second positive N_2 overlapped molecular emission spectra. *J. Phys. D: Appl. Phys.*, 37(14):1904–1916, 2004.

[52] C. O. Laux and C. H. Kruger. Arrays of radiative transition probabilities for the N_2 first and second positive, NO beta and gamma, N_2^+ first negative, and O_2 Schumann-Runge band systems. *J. Quant. Spectrosc. Radiat. Transfer*, 48(1):9–24, 1992.

[53] A. Lofthus and P. H. Krupenie. The spectrum of molecular nitrogen. *J. Phys. Chem. Ref. Data*, 6(1):113–307, 1977.

[54] G. Herzberg. *Molecular spectra and molecular structure: I. Spectra of diatomic molecules*. Van Nostrand Reinhold, New York, 1962.

[55] M. A. Linne. *Spectroscopic Measurement*. Adademic Press, 2002.

[56] J. M. Brown. *Molecular Spectroscopy*. Oxford University Press, 1998.

[57] A. Schadee. Unique definitions for the band strength and the electronic-vibrational dipole moment of diatomic molecular radiative transitions. *J. Quant. Spect. & Radiat. Trans.*, 19(4):451–453, 1978.

[58] R. W. Nicholls and A. L. Stewart. *Atomic and Molecular Processes edited by D. R. Bates*. Adademic Press Inc. (London) Ltd., 1962.

[59] I. Kovacs. *Rotational structure in the spectra of diatomic molecules*. New York, American Elsevier Pub. Co., 1969.

[60] *http://physics.nist.gov/PhysRefData/ASD/index.html*.

[61] M. A. Lieberman and A. J. Lichtenberg. *Principles of Plasma Discharges and Materials Processing*. John Wiley & Sons.

[62] A. Fridman and L. A. Kennedy. *Plasma Physics and Engineering.* New York, Taylor and Francis, 2004.

[63] J. Shang, S. T. Surzhikov, R. Kimmel, J. Menart, D. Gaitonde, and J. Hayes. Plasma actuators for hypersonic flow control. volume AIAA-2005-562 of *43rd AIAA Aerospace Sciences Meeting and Exhibit*, January 2005.

[64] T. Deconinck, S. Mahadevan, and L. L. Raja. Self-consistent two-dimensional simulations of glow discharge phenomena for high-speed flow control. volume AIAA-2006-372 of *44th AIAA Aerospace Sciences Meeting and Exhibit*, January 2006.

[65] S. Leonov, V. Bityurin, K. Savelkin, and D. Yarantsev. The features of electro-discharge plasma control of high-speed gas flows. volume AIAA-2002-2180 of *33rd AIAA Plasmadynamics and Lasers Conference*, May 2002.

[66] S. Leonov, V. Bityurin, and D. Yarantsev. The effect of plasma indced separation. volume AIAA-2003-3853 of *34th AIAA Plasmadynamics and Lasers Conference*, June 2003.

[67] R. L. Kimmel, J. R. Hayes, J. A. Menart, and J. Shang. Effect of magnetic fields on surface plasma discharges at Mach 5. volume AIAA-2004-2661 of *35th AIAA Plasmadynamics and Lasers Conference*, June-July 2004.

[68] D. M. Phillips. Determination of gas temperature from unresolved bands in the spectrum from a nitrogen discharge. *J. Phys. D: Appl. Phys.*, 8(3):507–521, 1975.

[69] S. T. Surzhikov and J. Shang. Two-component plasma model for two-dimensional glow discharge in magnetic field. *J. Comp. Phys.*, 199(2):437–464, 2004.

[70] D. Winske and M. E. Jones. Particulate dynamics at the plasma-sheath boundary in DC glow discharges. *IEEE Trans. Plasmas Sci.*, 22(4):454–464, 1994.

[71] G. S. Selwyn, J. S. McKillop, K. L. Haller, and J. J. Wu. *In situ* plasma contamination measurements by hene laser light scattering: A case study. *J. Vac. Sci. Technol. A*, 8(3):1726–1731, 1990.

Vita

Jichul Shin was born in Pusan, South Korean on Nov. 22, 1971 as the youngest son of Hyunsuk Shin and Eunhee Cho. He earned his bachelor's degree in Mechanical Engineering Department, INHA University in 1998. After his bachelor's degree, he worked as an assistant engineer in R&D center at LG Engineering company for three and a half years. In August 2001, he entered the graduate school of Aerospace Engineering and Engineering Mechanics Department, The University of Texas at Austin. He earned his master's degree in Engineering Mechanics on December 2003 under the supervision of Professor Dr. Raja. He started his doctoral research in January 2004.

Permanent address: Samick beach apt. 105-808
Namchun-2-dong Sooyoung-ku
Pusan, 613-751, South Korea

This dissertation was typeset with LaTeX[†] by the author.

[†]LaTeX is a document preparation system developed by Leslie Lamport as a special version of Donald Knuth's TeX Program.